Effect of temperature on the hydrodynamics of a fluidized bed circulating in a long tube for a solar energy harvesting application

Ronny Gueguen, Samuel Mer, Adrien Toutant, Françoise Bataille, Gilles Flamant

Effect of temperature on the hydrodynamics of a fluidized bed circulating in a long tube for a solar energy harvesting application

Ronny Gueguen[1], Samuel Mer[2], Adrien Toutant[2], Françoise Bataille[2], Gilles Flamant[1*]

[1] Processes, Materials and Solar Energy Laboratory, PROMES-CNRS, 7 Rue du Four Solaire, 66120 Font-Romeu, France

[2] Processes, Materials and Solar Energy Laboratory, PROMES-CNRS, University of Perpignan (UPVD), Tecnosud, Rambla de la Thermodynamique, 66100 Perpignan, France

[*] Corresponding author: Gilles.Flamant@promes.cnrs.fr; (+33)468307758

Abstract

The particle-in-tube solar receiver concept for solar towers uses fluidized particles as heat transfer fluids. The experiments are conducted with a single tube of aspect ratio H/D = 67 irradiated over a 1-m height using concentrated solar energy. Olivine particles of Geldart's Group A are used. Fluidization regimes are identified thanks to pressure signal analyses, and regime maps are plotted depending on the temperature in the range 150–700 °C. Both the local slip Reynolds number and the particle temperature govern the regime transitions. The limits and size of the turbulent fluidization regime domain decrease with temperature. The particle volume fraction also decreases with temperature. Finally, the intensity of the wall-to-particle heat transfer is discussed as a function of the fluidization regimes. As an indicator of the heat transfer intensity, a dimensionless coefficient is derived. This coefficient increases with temperature and exhibits the highest values for the turbulent fluidization regime.

Keywords: Particle-in-tube solar receiver; particle-driven CSP; fluidization regimes; upward dense particle circulation; heat transfer coefficient; hydrodynamics of gas–solid flow.

1. Introduction

1.1. Particles as heat transfer fluid for solar receivers

Concentrated solar power (CSP) produces electricity using a thermodynamic cycle. In CSP plants, particularly in solar towers, a heat transfer fluid (HTF) circulates in the receiver located at the top of a tower to absorb the concentrated solar radiation reflected by the heliostats field. The heat collected by the HTF can be stored to produce electricity on demand. The most commonly used HTF in commercial solar towers is molten salt, which has a temperature operation range between 220 and 565 °C. Below the lower limit, it solidifies; thus, constant electrical consumption is needed to maintain a threshold temperature in the pipe to prevent salt freezing (Castro-Quijada et al., 2022). In

contrast, the upper limit is a safety constraint due to the decomposition of molten salt (Zhang et al., 2017a).

One of the main objectives of the CSP industry is to decrease the cost of the plant. A pathway to achieve this goal is increasing its overall efficiency. An attractive solution consists of using highly efficient thermodynamic cycles, such as the supercritical CO_2 (sCO_2) cycle (Dunham and Iverson, 2014). However, these cycles require a high working temperature, above 650 °C, which is higher than the upper limit of the molten salt operation domain. A promising way to adapt the HTF to the targeted temperature is to use particles (Ho, 2016). Particles have a wide operation temperature range, are chemically stable and have generally low toxicity and cost (Zhang et al., 2017b).

Three main solar receiver technologies using particles as the HTF are currently under development at the prototype scale. Namely, the centrifugal receiver was designed by the German Aerospace Center (DLR), Germany (Ebert et al., 2019; Wu et al., 2014). Second, the falling particle receiver was designed by Sandia National Laboratory, USA (C. Ho et al., 2014; Ho et al., 2017) and the particle-in-tube receiver was developed by the French National Center of Scientific Research (PROMES, CNRS), France. In this concept, the particles are fluidized in a vessel named the "dispenser" and circulate upward inside vertical metallic tubes due to both a pressure gradient and a secondary air injection at the bottom of the latter. The particles are then indirectly heated, which limits their maximum reachable temperature by the tube thermal properties. Nevertheless, the tubular design is similar to molten salt receivers, which enables the use of a cavity to limit thermal losses (Behar et al., 2020; Gueguen et al., 2020). One of the main drawbacks of this concept is that several fluidization regimes can occur in this type of gas-particle suspension depending on the operation conditions, which considerably affect the thermal performance of the receiver (Kunii and Levenspiel, 1991).

Hence, several on-sun experimental studies were conducted based on the particle-in-tube solar receiver concept using Geldart's Group A particles fluidized at low air velocity, thus limiting the total air consumption of the plant. Silicon carbide particles (SiC) with a mean diameter of 63.9 µm were first used in a single tube receiver (Benoit et al., 2015; Flamant et al., 2013). Then, the solar receiver was upscaled to 150 kW and 16 tubes inside a cavity (Perez Lopez et al., 2016). The material was changed to olivine particles for the Next-CSP European project (Le Gal et al., 2023), accounting for a set of properties, such as thermal properties, toxicity and cost (Kang et al., 2019). Experiments were conducted with a single finned tube receiver, and a global heat transfer coefficient of 1200 ± 400 W/(m².K) was determined (Le Gal et al., 2019). However, in the previously cited experimental studies regarding the particle-in-tube receiver concept, all analyses on the fluidization regimes in the receiver tubes were simultaneously performed with the thermal measurements.

1.2. Fluidization regimes in the gas-particle fluidized bed

Fluidized beds have been used for decades in the chemical and petrochemical industries, mineral processing, and metallurgy (Fuchs et al., 2019). Depending on the solid and gas properties, the column geometry and the gas velocity, several fluidization regimes can occur in the column, resulting in various gas structure characteristics. They are detailed below for Geldart's group A particles and summarized in Figure 1.

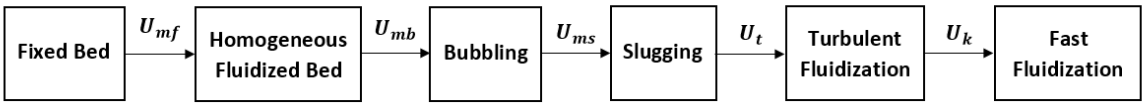

Figure 1: *Fluidization regimes for Geldart's group A particles at increasing superficial gas velocity.*

The minimum fluidization velocity, U_{mf}, is the threshold velocity at which the particles initially in the fixed bed become fluidized. The drag force of the upward gas is enough to compensate for both the gravity and the van der Waals forces between the particles, which acquire some fluid-like properties (Kunii and Levenspiel, 1991; Wu and Baeyens, 1991). The particles can be gathered in four Geldart groups as a function of their density and mean diameter, which classifies their ability to be fluidized (Geldart, 1973). (Leckner, 2017) compared the fluidization behavior of Group A and Group B particles. For Group A particles, increasing the gas velocity after the minimum of fluidization results in a dense and homogenous fluidization regime until bubbles appear in the bed. A maximum stable bubble size is reached when coalescence and scission are balanced. Bubbles merge into slugs at the velocity noted U_{ms} either by increasing the gas velocity (Baeyens and Geldart, 1974) or if the bubble size reaches approximately 60% of the column diameter (Kong et al., 2017). The slugs are initially large and slow elongated bubbles under the form of wall slugs (against the column walls), then evolve toward axisymmetric slugs (at the middle of the column), and finally as complete slugs (they occupy all the column cross section). Under wall-heating conditions, this regime is associated with a decrease in the heat transfer between the hot walls and the bed compared to the bubbling regime. Increasing the gas velocity again leads to the turbulent fluidization regime when the bubble scission completely compensates for their coalescence, it is identifiable by a maximum of the pressure fluctuations (Bi et al., 2000). In the fluidization literature, the velocity noted U_t is sometimes used to characterize either the choking phenomenon or the onset of the turbulent fluidization regime, as explained in (Bi et al., 1993). Hence, to avoid any confusion, the turbulent fluidization velocity is defined as U_t. In this regime, the chaotic air structures lead to vigorous particle mixing in a bed that is still relatively dense. The corresponding heat transfer rate is consequently larger than in the other regimes (Grace et al., 2020a). Finally, when the gas velocity reaches the particle terminal velocity or is up to several times this threshold value for small particles as in Group A, the fast fluidization regime occurs at a velocity of U_k (Grace et al., 2020b). The latter is characterized by a phase inversion. The gas phase turns into the continuous phase, while the particles are dispersed in the form of clusters and ejected outside of the column (Grace et al., 2020a). The commonly used circulating fluidized beds (CFBs), including risers, use this regime to cause the particles to circulate by applying high gas velocity at the bottom of the tubes (Boonprasop et al., 2019; Rahman et al., 2020). In CFBs, a transition region between dilute or core annular regimes and between the core annular and fast fluidization regimes are identified (Breault et al., 2020). Generalized regime maps for gas-solids and liquid-solids fluidization are proposed in (Sun and Zhu, 2021). The concept of a circulating-turbulent fluidized bed (C-TFB) was suggested to combine the advantages of the circulating fluidized bed and turbulent fluidized bed (Zhu and Zhu, 2008). A circulating bed at a relatively high solid concentration has been obtained, with uniform radial and axial distributions that improve particle mixing and local heat transfer (Sun and Zhu, 2019).

Several methods can be used to identify and characterize the fluidization regimes. High-speed cameras have been used to record the hydrodynamics within the bed (Shaffer et al., 2013). However, a solar receiver made of opaque tubes prevents the use of this technique. Furthermore, because of the particle opacity, this method can only record phenomena in the near wall region, even with transparent tubes. Acoustic methods have also been applied to characterize the fluidization regimes since particle–particle and wall-particle collisions imply vibrations that can be recorded and analyzed (Li et al., 2011). Although this is a noninvasive method for particle flow characterization, it suffers from a major drawback, namely, the cost of these thermally resistant devices (Villa Briongos et al., 2006). Positron emission particle tracking (PEPT) is another noninvasive method that consists of tracking the motion of a radioactive particle over a long period of time, called a tracer, using a camera (Tebianian et al., 2016; Van de Velden et al., 2008). While relatively precise, this method requires specific equipment limited in size and a high number of recorded events, i.e., high acquisition times. Optical fiber probes can also be used. The light reflected by bubbles or particles differs, which results in variations in the light received by the probe that can be further analyzed (Bi et al., 2000; Mokhtari and Chaouki, 2019). Here, the main drawback is the resistance of the probes (and of their sheath material) to high temperatures. Finally, another method using pressure measurements is the selected method for our study. Essentially, a gas structure, a bubble for example, is characterized by an overpressure at its top and a depression at its wake (Punčochář and Drahoš, 2005; Xie, 1997). Hence, it causes a succession of positive and negative peaks on a pressure signal when it flows near the corresponding probe. Since the structures are developed in the bed as distributions (in terms of size and velocity), the associated pressure signals show various frequencies and magnitudes that are distinctive features of the fluidization regimes and can be analyzed by signal processing methods (Johnsson et al., 2000; van der Schaaf et al., 2002).

Concerning modelling and simulation, the various approaches for swirling gas-particle flows simulation are reviewed in (Zhou, 2023); whereas (Nigmetova et al., 2022) proposed a three-dimensional DEM-CFD simulation (Lagrange-Euler approach) of a lab-scale fluidized bed and compared the results with the two-fluid model (Euler-Euler approach). (Benoit et al., 2018) have developed the first numerical simulation of the single-tube fluidized bed solar receiver using the two-fluid model.

1.3. Progress in the particle-in-tube solar receiver and objectives

In the particle-in-tube solar receiver concept, the particles circulate due to both an overpressure in the dispenser fluidized bed and a secondary air injection at the bottom of the tubes. This control strategy results in particle circulation as a dense suspension (i.e., particle volume fraction of 20–30%. Consequently, the wall-to-bed heat transfer rate is higher than that in classical CFB risers, where particle circulation is possible only at high air velocities and then at low particle volume fractions. Furthermore, the risers have a generally smaller aspect ratio (height over diameter) than solar receiver tubes because of their larger internal diameters. It is typically approximately 10 (Stefanova et al., 2011), while it is above 50 in the particle-in-tube receiver. Thus, a question arises: are the fluidization regimes encountered in classical fluidized beds occurring in these conditions? To answer this question, experimental and numerical studies with a single tube at ambient temperature have been performed. The associated main results are summarized in Table 1.

First, cristobalite particles of three different diameters, which all belong to Group A, were tested in a 2-m height tube of 0.05 m I.D. (internal diameter) (Kong et al., 2017). Without particle circulation, the bubbling to wall slugging transition was observed at 0.4–0.5 m height. Then, the

height of the tube was extended to 4 m. The transitions from bubbling to wall slugging and then to axisymmetric slugging were observed at approximately 1 m and 1.5 m, respectively. These experimental results have been compared to numerical simulations (Sabatier et al., 2020). Finally, the tube height was increased to more than 6 meters, with particle circulation, and the concept was to insert small tubes within the main receiver tube to break the slugs and create a turbulent fluidization-like regime (Deng et al., 2021). The obtained results validated the use of these inserts from the heat transfer point of view. However, the implementation of these inserts in hundreds of tubes for an upscaled solar receiver is problematic. Nevertheless, a comparison with bare tubes was performed, and the same regime transitions as in (Sabatier et al., 2020) were determined.

In the three above-cited studies regarding the fluidization regimes at ambient temperature (Deng et al., 2021; Kong et al., 2017; Sabatier et al., 2020), the superficial air velocity was limited to 0.30 m/s. Only bubbling and slugging regimes were observed. Furthermore, in earlier on-sun studies with the particle-in-tube solar receiver cited in the previous section (Benoit et al., 2015; Flamant et al., 2013; Le Gal et al., 2019; Perez Lopez et al., 2016), the superficial air velocities were limited to 0.11 m/s, which was even lower. Consequently, these were expected to operate mainly in the slugging regime, which was not the best regime with respect to heat transfer. Then, an additional experimental study was performed at ambient temperature, extending the superficial air velocity up to 0.54 m/s, which enabled the observation of the turbulent and fast fluidization regimes. The bubbling, slugging, turbulent and fast fluidization regimes were identified in the tube due to the pressure signal analyses resulting in establishing a complete diagram of the fluidization regimes in the specific conditions of the high aspect ratio tubes with particle circulation (Gueguen et al., 2022). In these experiments, transitions between slugging, turbulent and fast fluidization regimes did not occur along the tube height and only depended on the local slip velocity, U_{slip}. In contrast, in CFBs, core-annulus flow (CAF) could coexist with a turbulent fluidized bed at the bottom of the riser (Zhang et al., 2015). Our previous studies confirmed that the slip velocity is the pertinent indicator of the turbulent and fast fluidization regime in the pressure-driven suspension, as in the case of circulating fluidized beds (Bi and Grace, 1995; Rabinovich and Kalman, 2011). However, the critical velocities for the regime transitions were significantly lower than in the classical CFB, mainly due to the operating mode of the receiver using pressure as a control parameter.

The fluidization regime diagram obtained in an earlier study is presented in Figure 2. It is plotted in terms of dimensionless quantities: the ratio of the height over the internal diameter of the tube versus the slip velocity expressed as a particle slip Reynolds number (Gueguen et al., 2022). A comparison of the data from the other studies is provided in Table 1. The associated slip velocities were estimated according to the data of the air velocities, particle mass fluxes and particle volume fractions provided by the authors. Figure 2 shows that the bubbling to wall slugging regime transition identified by (Kong et al., 2017) (in blue) corresponds well to the bubbling and transition zone of the diagram. Furthermore, the wall slugging regime zones determined by (Deng et al., 2021; Sabatier et al., 2020) (in red and green, respectively) are mainly located in the slugging region of the diagram. Clearly, the turbulent fluidization regime was not reached in these previous experiments.

Table 1: *Comparison between the studies regarding the fluidization regimes performed with the particle-in-tube solar receiver concept and a single tube at ambient temperature.*

References	Particles	d_{sv} (µm)	D_t (mm)	H_t (m)	U_{air} (m/s)	G_p (kg/(m².s))	Comments

Kong et al., 2017	Cristobalite	35.4; 55; 75	50	2	0.04–0.30	0	Bubbling to wall slugging transition between 0.4 and 0.5 m height
Sabatier et al., 2020	Cristobalite	35.4; 55; 75	50	4	0.02–0.22	0	Bubbling to wall slugging transition at 1 m height, and to axisymmetric slugs at 1.5 m
Deng et al., 2021	Cristobalite	55	50	6.6	0.11–0.22	56–175	Use of BRP to break slugs. With bare tube, bubbling to wall slugging and then to axisymmetric slugging detected at, respectively 1 and 1.5 m height
Gueguen et al., 2022	Olivine	61	45	3.6	0.01–0.54	0–392	Observation of turbulent and fast fluidization regimes. Comparison of experimental data and simulation results Diagram of the regimes governed by the slip velocity Figure 2. Slugging transitions at various height depending on the velocity.

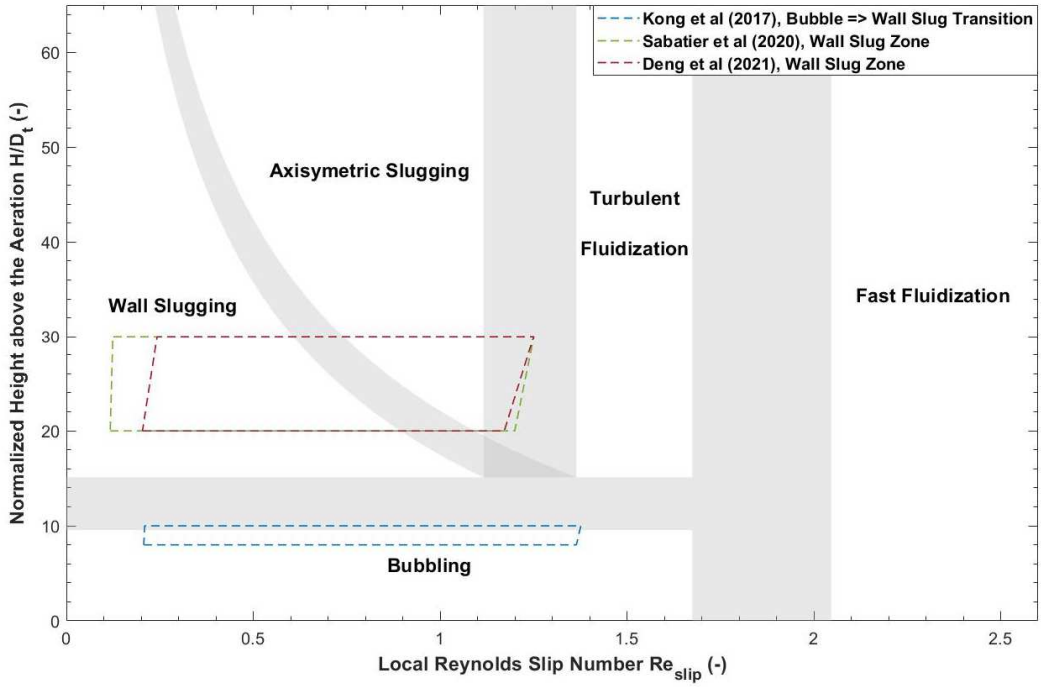

Figure 2: *Simplified diagram of the fluidization regimes and their transition zones determined at ambient temperature and comparison with literature data for the particle-in-tube solar receiver concept (Gueguen et al., 2022). The bubbling to wall slugging transition (blue) and wall slugging zone (green and red) identified by (Kong et al., 2017) and (Deng et al., 2021; Sabatier et al., 2020) correspond well to the diagram.*

The scientific literature is very limited regarding the influence of the temperature on the transitions of the fluidization regimes. Studies have been published mainly on the minimum of fluidization, which decreases with the temperature for Group A particles (Wu and Baeyens, 1991).

The fluidization regime diagrams are generally plotted in terms of the Archimedes number (Ar) calculated at ambient temperature (Grace et al., 2020b; Rabinovich and Kalman, 2011; Yerushalmi and Cankurt, 1979). The latter enables the consideration of particles with various mean diameters. In these diagrams, the transitions of the onset and the termination of the turbulent fluidization regime both decrease with Ar due to the decrease in the mean particle diameter (d_{sv}).

Based on the previous context, the main objective of this paper is to extend the earlier study carried out at ambient temperature to higher temperatures (up to approximately 700 °C) to determine the effect of temperature on the transitions between the fluidization regimes in the particle-in-tube solar receiver concept. The experimental setup is initially presented as along with the calculated quantities and the methods of the pressure signal analyses used to identify the fluidization regimes. The results regarding the regimes and particle volume fraction as a function of temperature are then presented. A discussion on the effect of the temperature on fluidization regimes and of the fluidization regimes on the global heat transfer coefficient is proposed at the end of the paper.

2. Experimental setup

2.1. Particles

Olivine was selected as the heat transfer and storage medium in the framework of the European Next-CSP project ("Next-CSP Project: High Temperature Concentrated Solar Thermal Plant with Particle Receiver and Direct Thermal Storage," 2020). It is a silicate sand, mostly composed of MgO, SiO_2 and Fe_2O_3, and has attractive thermomechanical, health and cost properties (Kang et al., 2019). The particles are expected to belong to Group A of the Geldart classification (Geldart, 1973) that enables their fluidization at low air velocity followed by a reduction in the associated air consumption and auxiliary power loss. Figure 3 plots the position of the selected particles in the Geldart classification, according to (Kong et al., 2017).

The particle size distribution of the olivine sample was determined by laser diffraction using a Malvern Mastersizer 3000 granulometer. The Sauter mean diameter, d_{sv}, is the diameter of the sphere that has the same surface/volume ratio as the particle (Dodds and Baluais, 1993). The latter diameter is generally used in fluidization because it accounts for the surface phenomena and the presence of fine particles that can degrade the fluidization quality because of their cohesive properties. It has been calculated over the entire distribution at 61 µm. With a bulk density ρ_{part} of 3300 kg/m^3, the powder belongs to Group A of the Geldart classification, as shown in Figure 3 by the black square.

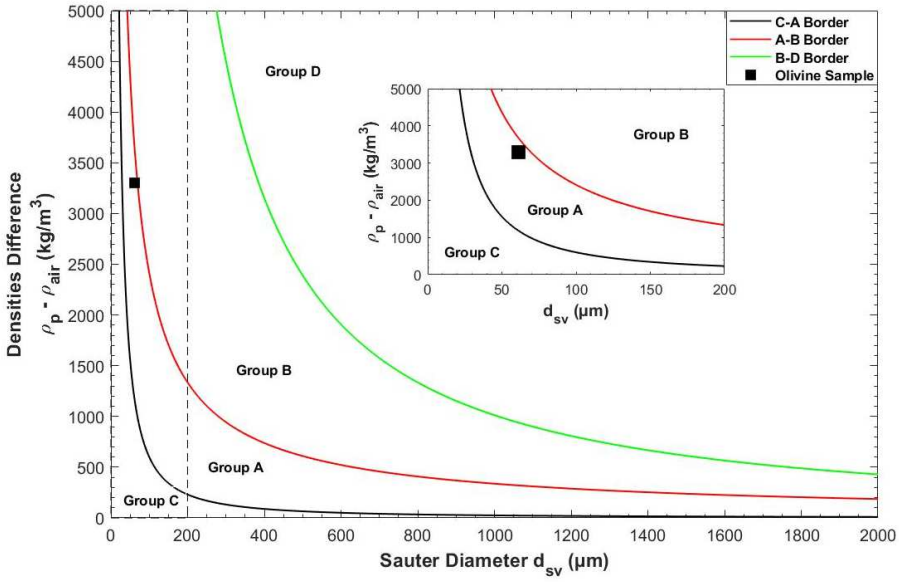

Figure 3: *Position of the olivine sample on the Geldart classification (Geldart, 1973; Kong et al., 2017). The subfigure corresponds to a zoomed image of the dashed rectangle, and the position of the sample is represented by the black square.*

The minimum fluidization and bubbling velocities that characterize the powder sample have been experimentally determined with a 9 cm I.D. fluidization column. The classical pressure drop versus the superficial air velocity method was used, leading to values for U_{mf} and U_{mb} of respectively (4.2 ± 0.3).10^{-3} m/s and (5.7 ± 0.4).10^{-3} m/s. These values were in good agreement with the correlations of (Wu and Baeyens, 1991) and (Abrahamsen and Geldart, 1980), which were respectively (4.0 ± 0.8).10^{-3} m/s and (6.2 ± 0.1).10^{-3} m/s. More details regarding the powder characterization can be found in (Gueguen et al., 2021).

2.2. Solar receiver description

The experimental setup is schematically represented in Figure 4a. The olivine particles are fluidized in a 0.36 m² vessel called a "dispenser" by an air flow rate fixed at 10.6 sm^3/h, which correspond to a superficial air velocity of 9.7.10^{-3} m/s that is 1.7 times the minimum bubbling velocity at ambient temperature, to obtain a homogeneous freely bubbling regime. The receiver tube is plunged inside the fluidized bed. A leak valve controls the total pressure in the dispenser. The particles flow upward in the tube due to the pressure difference between the bottom and the top (at ambient pressure). A secondary air flow rate, named "aeration," is injected 50 cm above the tube tip. The flow becomes stabilized, as demonstrated by (Boissiere et al., 2015) and the fluidization regimes in the receiver tube can be controlled (Gueguen et al., 2022).

The receiver tube is made of Inconel 601®. It has a 48-mm internal diameter D_t (i.e., 0.0018 m² internal surface area S_t) and is 3-mm thick with a height of 3.20 m. The tube is irradiated due to the concentrated solar power over a 1-m height irradiated zone, identified in yellow in Figure 4a. It is painted with Pyromark® to increase its absorption in the solar spectrum (C. K. Ho et al., 2014). The solar receiver is positioned at the focus of the 1-MW solar furnace of Odeillo (France) (Guillot et al., 2018; Trombe and Le Phat Vinh, 1973). The various solar flux configurations used during the experimental campaign are provided in Supplementary Information SI-1. To reduce the thermal

losses and reflect the concentrated solar beam, a ceramic cavity surrounds the tube, as shown in Figure 4b.

When the total pressure is high enough, the particles flow in a tank located on a weighing scale to measure the exit particle mass flow rate. To maintain stationary conditions during the experiments, the dispenser is fed with particles from a storage tank due to a rotary valve.

In terms of instrumentation, eleven pressure probes are implemented in the system. In the dispenser, they measure both the total pressure P_{tot} and the pressure drop through the fluidized bed. In the tube, the probes, named P_i in red in Figure 4, are connected to differential and relative pressure sensors. This enables the calculation of the local particle volume fraction and identification of the fluidization regimes, as detailed in Section 3. The setup also contains thermocouples. According to (Grace et al., 2020c), the heat exchange between the air and the particles is very efficient in a fluidized bed. Consequently, only a few millimeters are needed to balance particle and air temperatures. Then, the temperature provided by an internal thermocouple in the tube can be considered as the temperature of both the air and particles. Three thermocouples are located in the dispenser to measure the particles' temperature T_{disp}. Furthermore, all along the receiver tube, 32 externally welded and 24 internal thermocouples are regularly spaced and identified in red and blue, respectively, in Figure 4. Three cross-sections of the tube are particularly well arranged, as shown in Figure 4c. They are located at the inlet, middle and outlet of the irradiated zone. The detailed positions of the pressure probes and thermocouples are provided in Supplementary Information SI-2.

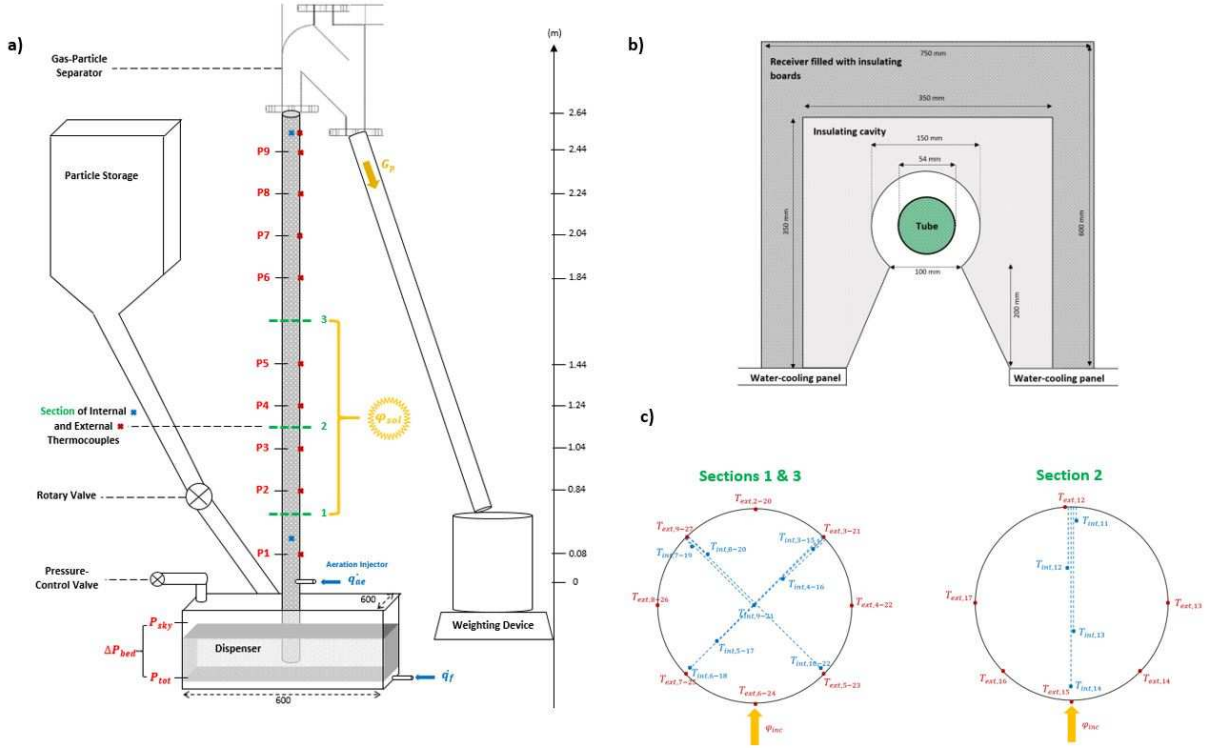

Figure 4: *Schematic representation of a) the receiver tube and its instrumentation, b) its cavity, and c) the three tube cross-sections at 0.6, 1.1 and 1.6 m heights.*

3. Background

3.1. Control of the solar receiver

3.1.1. Operating parameters

The control parameters of the solar receiver are the total pressure in the dispenser, P_{tot}, i.e., the driving force of the system; the aeration flow rate $\dot{q_{ae}}$, which corresponds to a superficial air velocity at the height of the aeration injection, U_{air}; the incident solar flux density at the entrance of the cavity, φ_{sol}; and the particle temperature in the dispenser, T_{disp}. The combination of these parameters leads to a gas-particle suspension flowing at a given particle flow rate, temperature and particle volume fraction.

First, the particle mass flux, noted G_p (in kg/(m^2.s)), is the ratio of the particle mass flow rate (in kg/s) over the internal section of the tube. It is calculated by linear regression of the temporal particle mass weight recorded by the scale during the acquisition time. The associated uncertainty is due to both the precision of the scale and the regression error. Second, the particle temperature at the outlet of the receiver, T_{part}^{out}, is essential to calculate its thermal performance. It is defined as the average of the temperatures measured within the tube at the outlet of the irradiated zone (i.e., at 1.6 m height): $T_{part}^{out} = \left(T_{int,16} + T_{int,17} + T_{int,21}\right)/3$, where the thermocouples are located at radial positions of $D_t/3$, $D_t/2$ and $2D_t/3$ (cf. Figure 4c).

The variation ranges of the operating parameters during the experimental campaign are detailed in Table 2. In on-sun conditions, increasing the particle mass flux leads to a decrease in the particle outlet temperature, as illustrated in Figure 5. To increase T_{part}^{out} at a given particle mass flux, the incident solar power (represented by markers and colors in the figure) can be increased or the particles in the dispenser (empty points) can be preheated.

Table 2: *Variation ranges of the operating parameters of the setup in the reported experiments.*

Operating Parameter	P_{tot} **(mbar)**	$\dot{q_{ae}}$ **(sm³/h)/** U_{air} **(m/s)**	T_{disp} **(°C)**	φ_{sol} **(kW/m²)**	G_p **(kg/(m².s))**	T_{part}^{out} **(°C)**
Range	145–380	0.1–2.5/ 0.025–0.469	T_{amb} – 297	211–531	0–93	130–677

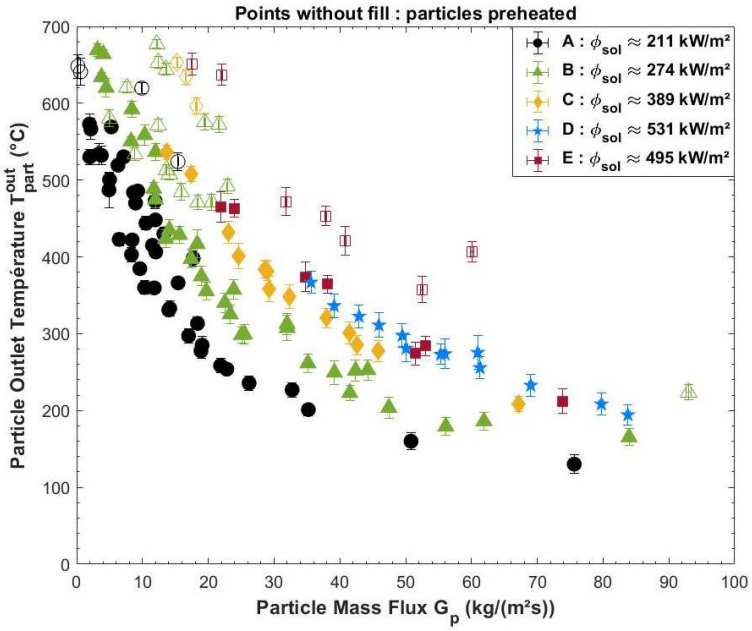

Figure 5: *Evolution of the particle outlet temperature as a function of particle mass flux. The tube is irradiated by the concentrated solar beam over a 1-m long section with various incident solar flux densities. The empty markers correspond to preheated particles in the dispenser up to ~300 °C.*

3.1.2. Macroscopic quantity evolutions

The evolution of the pressure and temperature with the receiver tube height and radius were determined. An example was proposed using an aeration flow rate of 0.41 sm^3/h, a total pressure in the dispenser of 343 mbar and a particle mass flux of 50 kg/(m².s). The mean solar flux density was 519 kW/m².

Figure 6 shows radial temperature profiles. Each color is representative of the height of a well-arranged section of the tube (cf. Figure 4) where this profile can be measured. The negative radius values correspond to the irradiated face of the tube, and the vertical black dashed lines represent the tube thickness. The particle temperature within the tube is very homogeneous at a given height (radial profile), which results in very good particle mixing specific to the fluidized beds, regardless of the fluidization regime. Hence, the mean particle temperatures can be calculated accurately at the inlet, middle and outlet of the irradiated zone of the receiver tube. Even near the irradiated tube wall, the thermal gradient in the particle flow is not detected at a distance of 2 mm from the internal tube wall.

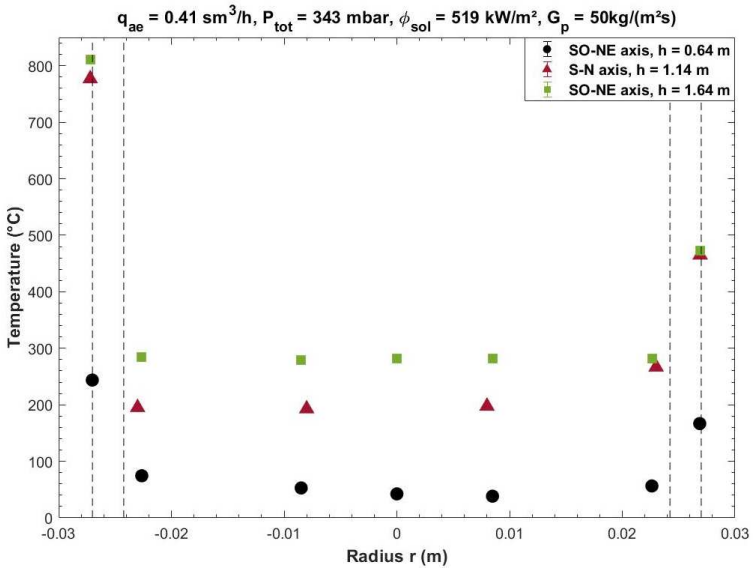

Figure 6: *Example of radial temperature profiles at three heights: 0.64 m (black), 1.14 m (red) and 1.64 m (green). The tube thickness is represented by vertical black lines.*

Considering the variations in pressure and temperature with height, the local superficial air velocity, $U_{air,i}$, is also modified. It can be calculated by Equation (1) considering air as an ideal gas. In this equation, P_i and T_i are the local pressure and temperature measured within the receiver tube, respectively, while the subscript "ae" refers to the quantities measured at the level of the aeration injection. Then, the air velocity increases with height due to both the decrease in pressure and the increase in temperature.

$$U_{air,i} = \frac{\dot{q_{ae}}}{S_t}\frac{P_{ae}}{P_i}\frac{T_i}{T_{ae}} \quad (1)$$

The particle volume fraction, α, is the proportion of the volume actually occupied by the particles in a given volume of the suspension (Geldart, 1986). It can be calculated due to the measurement of the pressure drop ΔP for a given height Δh. According to (Gueguen et al., 2022; Zhang et al., 2017b), the total pressure drop due to particle acceleration and friction represent less than 3 % of the measured pressure drops. Hence, they are neglected in the calculation of α that is only due to the effective weight of the suspension (Equation (2)). It is an average value over time since the pressure sensors used have a long response time. The uncertainty associated with the differential pressure sensors is $\delta(\Delta P) = 0.05$ mbar. Consequently, the uncertainty in the particle volume fraction, $\delta\alpha$, is low (Equation (3)).

$$\alpha = \frac{\Delta P}{(\rho_{part} - \rho_{air})g\Delta h} \quad (2)$$

$$\delta\alpha = \alpha\left(\frac{\delta(\Delta P)}{\Delta P} + \frac{\delta(\Delta h)}{\Delta h}\right) \quad (3)$$

Our earlier study at ambient temperature concluded that the slip velocity, U_{slip}, is a pertinent indicator of the fluidization regime transitions in our system (Gueguen et al., 2022). The slip velocity is the difference between the interstitial velocity of the air and the velocity of particles, account for the particle volume fraction (Equation (4)). Furthermore, a particle slip Reynolds number can be calculated with Equation (5) to consider the viscous effects. Its calculation requires the air density and viscosity, respectively, ρ_{air} and μ_{air}, which depend on the pressure and temperature (Holman, 2002; Incropera et al., 2007). Details of their calculations are provided in Supplementary Information SI-3.

$$U_{slip} = \frac{U_{air}}{1-\alpha} - \frac{G_p}{\rho_{part}\alpha} \tag{4}$$

$$Re_{slip} = \frac{\rho_{air} U_{slip} d_{sv}}{\mu_{air}} \tag{5}$$

Therefore, these new derived quantities are used in the following sections for illustrating the experimental results.

3.2. Methods of identification of the fluidization regimes

3.2.1. Signal processing methods

This section summarizes the signal processing methods used to identify the fluidization regimes in the particle-in-tube solar receiver concept based on pressure measurement. More details are provided in (Gueguen et al., 2021).

The first method, in the temporal domain, is the calculation of the cross-correlation function between two relative pressure signals in the tube (Fan et al., 1983; Johnsson et al., 2000). Let us consider two signals of N_{acq} points, P_i and P_{i+1}, recorded at successive heights in the tube and at an acquisition frequency f_{acq}. The principle of this method is based on applying a time lag τ_{lag} at the lower pressure signal (i.e., recorded higher in the tube) and to calculate the cross-correlation function between the two signals, $CC_{i,i+1}$ (Eq.(6)). Here, both the shape of the function $CC_{i,i+1} = f(\tau_{lag})$ and the value of τ_{lag}, which corresponds to the maximum of the function, are characteristics of the fluidization regimes.

$$CC_{ii+1}(\tau_{lag}) = \frac{1}{N_{acq} - \tau_{lag} f_{acq}} \sum_{n=1}^{N_{acq}-\tau_{lag}f_{acq}} P_i(n) P_{i+1}(n + \tau_{lag} f_{acq}) \tag{6}$$

The second method, in the frequency space, applies a fast Fourier transform on the ith pressure signal P_i, then noted F_i, to obtain the associated power spectrum density (PSD), ϕ_{ii} (Bi, 2007; Johnsson et al., 2000). It is given by Equation (7). The pressure signal is split into M_{groups} of

N_{pts} each to reduce noise and highlight the relevant frequencies of the air structures. The PSD of each group is calculated and averaged to obtain ϕ_{ii} (the average is identified by $\langle F \rangle$ in the equation). The coherence analysis proposed by (van der Schaaf et al., 2002) reduces the effect of noise in the signal by calculating the cross power spectral density (CPSD), ϕ_{i0}, between the ith pressure signal and a reference signal, denoted "0" (Eq.(8)). Then, if the signals are similar at a given frequency, the CPSD is high. This is very similar to the cross-correlation function in the frequency space. Since ϕ_{i0} is a complex value, the authors (van der Schaaf et al., 2002) also define the coherence term, γ_{i0}^2 (Eq.(9)).

$$\phi_{ii}(f) = \frac{1}{N_{pts}} \langle F_i(f) F_i^*(f) \rangle \tag{7}$$

$$\phi_{i0}(f) = \frac{1}{N_{pts}} \langle F_i(f) F_0^*(f) \rangle \tag{8}$$

$$\gamma_{i0}^2(f) = \frac{\phi_{i0}(f)\phi_{i0}^*(f)}{\phi_{ii}(f)\phi_{00}(f)} \tag{9}$$

The coherence term can finally be multiplied by the initial PSD to obtain a coherent spectrum that exhibits a common phenomenon between the two pressure signals. In the same way, the opposite of the coherence term allows extracting the different phenomena between the signals in a new "incoherent" spectrum, IOP_{i0} (Eq.(10)). Selecting the pressure recorded in the dispenser (P_{tot}) as the reference enabled the reduction of the noise in the signals (Gueguen et al., 2021). Some information can be identified from this new spectrum, as explained in the next section.

$$IOP_{i0}(f) = \phi_{ii}(f)\left(1 - \gamma_{i0}^2(f)\right) \tag{10}$$

A classical method of signal processing consists of using the signal-to-noise ratio, SNR (Price and Goble, 1993). It consists of dividing integrals of the spectrum (i.e. powers of the spectrum) into two relevant frequency ranges. With this same concept the bubbles and wall slugs are characterized by frequencies above 1 Hz (Kong et al., 2017; Sabatier et al., 2020), and the axisymmetric slugs, turbulent and fast fluidization regimes are characterized by frequencies smaller than 1 Hz (Gueguen et al., 2021). Thus, a "signal-to-noise" ratio can be extracted from the incoherent part of the pressure signal, as shown by Equation (11). Then, the negative values of SNR (expressed in decibels) are representative of bubbles and wall slugs, as shown in the next section. According to Parseval's theorem, the power of a signal is conserved in the frequency and temporal spaces (Plancherel and Leffler, 1910). Then, the integral of IOP_{i0} and its evolution with height provide the same information as the relative pressure fluctuations (Gueguen et al., 2021). The SNR is more relevant in our case.

$$SNR_i = 10 \log\left(\frac{\int_{f=0}^{1} IOP_{i0}(f)df}{\int_{f=1}^{10} IOP_{i0}(f)df}\right) \tag{11}$$

Finally, both the value of the particle volume fraction and the shape of its evolution with height are representative of the fluidization regime (Gueguen et al., 2022, 2021).

3.2.2. Characteristics of the fluidization regimes

This section presents the results obtained with the pressure signal analyses described above to identify the fluidization regimes in the receiver tube. They are gathered in three configurations, where transitions can occur with respect to the tube height: bubbling/slugging, bubbling/turbulent fluidization and fast fluidization. The transition between these configurations is only possible with a change in the experimental parameters.

First, the parameters related to the processing methods need to be fixed to perform the identification. According to Shannon's theorem, the maximum detectable frequency in a PSD is half of the acquisition frequency (Shannon, 1949). Bubbles and wall slugs with typical frequencies above 1 Hz but not exceeding 10 Hz and an acquisition frequency $f_{acq}$of 20 Hz were selected for the experiments. Then, an earlier study on the identification of fluidization regimes showed that dividing the signals into 4 groups of 1024 points each was sufficient to identify the fluidization regimes (Gueguen et al., 2021).

The bubbling/slugging regime: Figure 7 presents a representative test performed with an aeration flow rate of 0.41 sm^3/h (i.e., a superficial air velocity at the aeration height of 0.09 m/s), a pressure in the dispenser of 272 mbar and an incident solar flux density of 207 kW/m^2 (i.e., a power of 20.7 kW). These parameters correspond to a particle mass flux of 15.4 $kg/(m^2.s)$ and a particle outlet temperature of 524 °C. Figure 7a shows the result of the coherence analysis at the first pressure signal, at 0.08 m above the aeration injection. The bubbling regime is identified in the spectrum by frequencies higher than 1 Hz and very low magnitudes (van der Schaaf et al., 2002). Due to this proximity to the aeration, the bubbling regime is identified for all tests at this height. Consequently, it is not observed in the following results. Then, Figure 7b shows the coherence analysis at the level of the 4^{th} relative pressure signal, recorded at 1.2 m height. The spectrum is representative of the axisymmetric slugging regime, characterized by marked peaks with dominant frequencies below 1 Hz and medium magnitudes (Deng et al., 2021; Kong et al., 2017). There are almost no frequencies recorded above 1 Hz, which indicates that there are no more bubbles or wall slugs. The characteristic frequency of 0.59 Hz is well representative of axisymmetric slugs. Notably, a peak is observed at 0.25 Hz, which could also be characteristic of a slug due to their distributions.

Figure 7c shows the cross-correlation function between the 4^{th} and 5^{th} relative pressure signals, i.e., between 1.2 and 1.4 m height. Normalized by the maximum of the function, a peak at a time lag of 0.2 s can easily be identified. This corresponds to the time needed by the air structure to flow between the two pressure probes at an upward velocity of 1.0 m/s. This velocity correlates well to the slugging regime according to the two-phase theory of fluidization (Deng et al., 2021; Fan et al., 1983). Finally, Figure 7d shows the evolutions with height of quantities that enable the identification of the fluidization regime. The irradiated height of the tube is represented in the figure with the vertical dashed lines. The first quantity is the particle volume fraction (in red), which is roughly constant, with a mean value of 0.274. The second quantity is the signal-to-noise ratio (black), as explained in Section 3.2.1. The first point at the lowest height, which corresponds to the $P1$ signal, is negative; here, the "noise" of the signal with frequencies above 1 Hz is dominant. This is

characteristic of the bubbling regime. The value is positive higher in the tube; thus, the transition through axisymmetric slugs occurred.

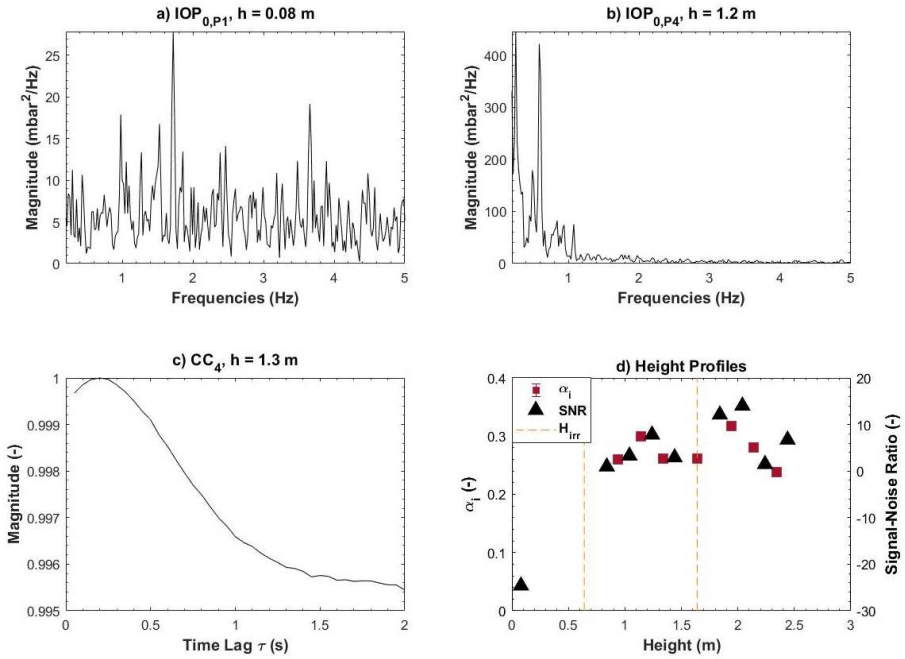

Figure 7: *Representative test of the bubbling/slugging configuration, performed with $\dot{q_{ae}} = 0.41$ sm³/h, $P_{tot} = 272$ mbar and $\varphi_{sol} = 207$ kW/m², corresponding to $G_p = 15.4$ kg/(m².s) and $T_{part}^{out} = 524$ °C.*

The bubbling/turbulent fluidization regime: Figure 8 presents a representative test with an aeration flow rate of 0.81 sm³/h (i.e., a superficial air velocity at the aeration height of 0.16 m/s), a pressure in the dispenser of 271 mbar and an incident solar flux density of 256 kW/m² (i.e., a power of 25.6 kW). These parameters correspond to a particle mass flux of 25.5 kg/(m².s) and a particle outlet temperature of 300 °C. As explained above, the first pressure sensors are too close to the aeration injection, and the regime detected at this position is always bubbling. Then, Figures 8a and b show the spectra obtained by coherence analysis of the second and fourth relative pressure signals, respectively, recorded at heights of 0.84 and 1.2 m. Different from the slugging regime, the spectra exhibit a quasi-plateau of frequencies below 1 Hz. They are associated with very high magnitudes, much higher than those in the slugging regime. No dominant frequency can be extracted from these spectra, which show the chaotic mixing characteristic of the turbulent fluidization regime (Bi et al., 2000).

Figure 8c plots the evolution of the cross-correlation function between P_4 and P_5. The shape of the function is different than in the case of the slugging regime, and the velocity provided by the maximum time lag does not correspond to the two-phase theory for slugs. Finally, Figure 8d indicates that the signal-to-noise ratio is negative for the first point, i.e., bubbling as explained above, and then increases with height until the last sensors, where it decreases but remains positive. This trend at the end of the tube is due to the high fluctuations at the surface of the suspension, which increase the "noise" in the spectra, i.e., frequencies measured above 1 Hz, and then decrease the value of the SNR. Furthermore, the particle volume fraction remains roughly constant with height, with a high value of 0.296.

Comparing Figure 7d and Figure 8d, it is surprising that particle volume fractions are very similar despite the variation of regimes. This result can be explained by the variation of the experimental parameters. In Figure 7, the temperature is 524°C whereas in Figure 8 it is 300°C, the corresponding solid mass flux being 15.4 and 25.5 kg/(m².s) respectively. Since the particle volume fraction decreases with the flow temperature and increases with the particle mass flux, the effects cumulate to rise the particle volume fraction in the turbulent regime at the level of the typical value for the bubbling-slugging regime.

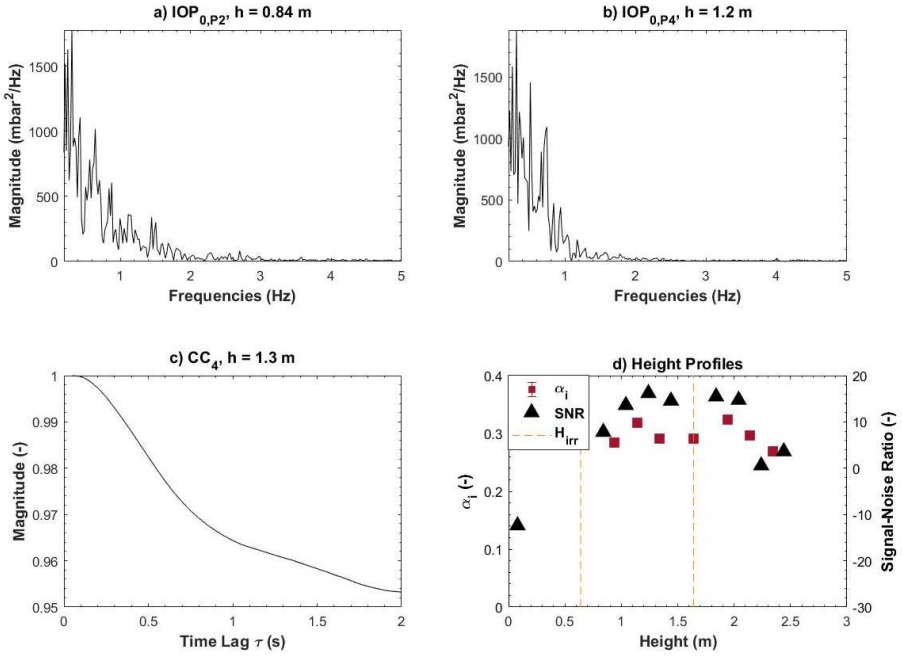

Figure 8: *Representative test of the bubbling/turbulent fluidization configuration, performed with* $\dot{q_{ae}} = 0.81$ *sm³/h,* $P_{tot} = 271$ *mbar and* $\varphi_{sol} = 256$ *kW/m², which corresponds to* $G_p = 25.5$ *kg/(m².s) and* $T_{part}^{out} = 300$ *°C.*

The bubbling/fast fluidization regime: Figure 9 presents a representative test of the fast fluidization regime, performed with an aeration flow rate of 1.44 sm³/h (i.e., a superficial air velocity at the aeration height of 0.29 m/s), a pressure in the dispenser of 165 mbar and an incident solar flux density of 282 kW/m² (i.e., a power of 28.2 kW). These parameters correspond to a particle mass flux of 15.9 kg/(m².s) and a particle outlet temperature of 485 °C. As expected, the first pressure signal is associated with the bubbling regime. Figure 9a shows the spectrum obtained by coherence analysis of P_2. It is characterized by a strong dominant frequency at 0.606 Hz and high magnitude on the same order as that for the turbulent fluidization regime. Furthermore, there are some other peaks at 0.47 and 0.74 Hz that are still associated with high magnitudes. This distribution is due to the strong mixing of the suspension. A question arises based on the spectrum: is the regime a turbulent fluidization at the bottom and a core annulus above (Zhang et al., 2015)? Nevertheless, its shape is also different from those of the turbulent fluidization regime. These peaks are actually characteristics of the upward flow of particle clusters, representatives of the fast fluidization regime (Johnsson et al., 2000). Furthermore, this regime is characterized by a relatively dense phase at the bottom of the suspension and a decrease in the particle volume fraction with height. The P_4 spectrum at a height of 1.2 m is characteristic of this dilute phase (Figure 9b). The shape of the spectrum is globally similar to

the previous one, but the magnitudes are much lower. The magnitudes decrease with increasing height, as indicated by the evolution of the signal-to-noise ratio in Figure 9d.

The shape of the cross-correlation function in Figure 9c is very similar to the turbulent fluidization regime. Finally, the evolution of the particle volume fraction in Figure 9d also shows the presence of the dilute zone at the top of the suspension. The strong decrease is characteristic of the fast fluidization regime. The mean value is 0.164, which is much lower than those in the other fluidization regimes.

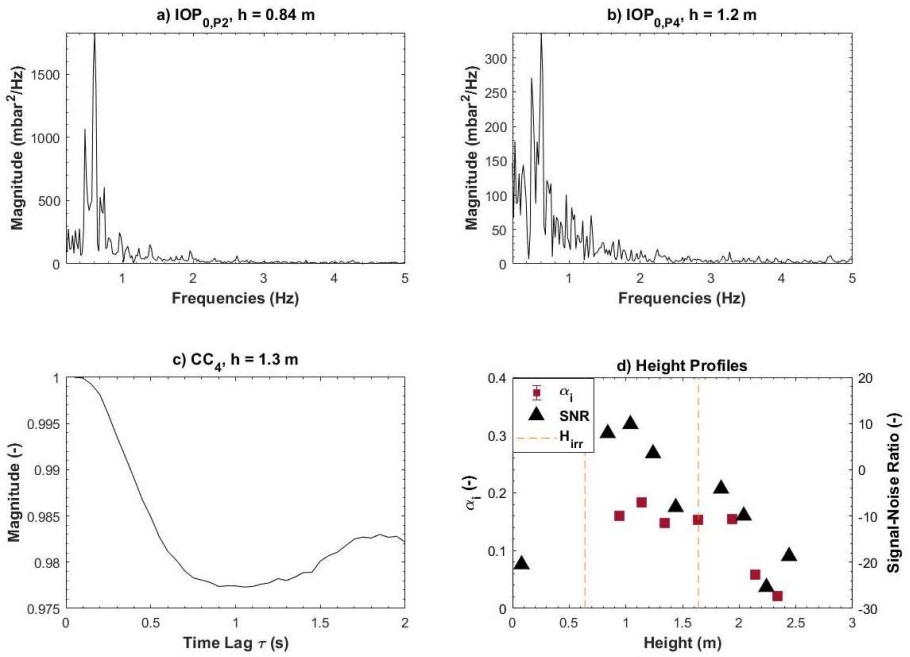

Figure 9: *Representative test of the bubbling/slugging configuration, performed with $\dot{q_{ae}} = 1.44$ sm³/h, $P_{tot} = 165$ mbar and $\varphi_{sol} = 282$ kW/m², which corresponds to $G_p = 15.9$ kg/(m².s) and $T_{part}^{out} = 485$ °C.*

The figures presented in this section have been selected for representative cases of each fluidization regime. The identification may be difficult because the steady state is not always perfectly satisfied, and multiple noise factors are due to the experimental facility, including the solar furnace itself. Consequently, the identification of the fluidization regimes is more difficult than in the earlier study at ambient temperature; however, it is still possible due to all of the processing methods and their comparison.

4. Results

4.1. Fluidization regimes as a function of temperature

A total of 196 tests were performed during the experimental campaign under stationary conditions in terms of particle mass flux, pressure and temperature. For each test, nine relative pressure signals are recorded in the receiver tube. Bubbling, wall slugging, axisymmetric slugging, turbulent fluidization and fast fluidization regimes were identified.

To determine a complete diagram of the fluidization regimes in the same way as at ambient temperature (cf. Figure 2), the regimes can be plotted as a function of the height and of the operating parameters. After several trials concerning the pertinent operating parameters to use (superficial air velocity as for classical fluidized beds, slip velocity as for CFBs, ratio of air velocity over the minimum fluidization velocity, and others), the local slip Reynolds number, Re_{slip}, was selected since it led to the best coherence between the experimental results. Several diagrams need to be created to assess the influence of temperature on the fluidization regimes. They are identified by the mean particle temperature in the irradiated zone of the receiver, $T_{part,irr}$, which varies between 150 and 700 °C.

The established diagrams are shown in Figure 10, where the markers and colors are representative of the fluidization regimes. The number of points plotted in each diagram is specified in the titles and varies between 110 and 248 points. Due to the temperature variation and the limits in the operation conditions, the same range of Re_{slip} was not reached for every temperature. Furthermore, although the slip velocity, or its associated Reynolds number, is used in CFB systems to determine regime transitions, it is generally not used in classical fluidized beds. However, it was selected since it enabled the points to gather in the regimes zones.

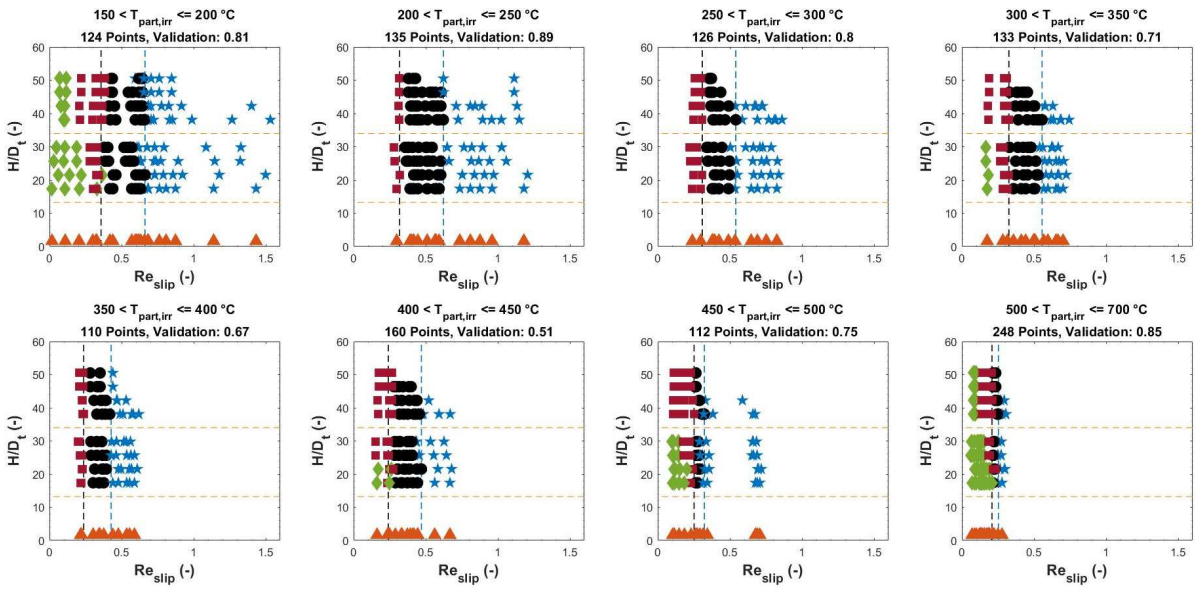

Figure 10: *Diagrams of the fluidization regimes encountered in the solar receiver tube and their transitions with height for eight ranges of the mean particle temperature in the irradiated zone. The fluidization regimes are identified by color: bubbling (orange), wall slugging (green), axisymmetric slugging (red), turbulent fluidization (black) and fast fluidization (blue).*

Then, Figure 10 shows that the bubbling regime (orange) is always identified at the height of the first sensor due to its proximity to the aeration injection. Furthermore, fast fluidization (blue) is observed for high values of Re_{slip}, turbulent fluidization (black) is observed for medium values, and slugging is observed for the lowest values. In the latter, wall slugs (green) and axisymmetric slugs (red) can be distinguished.

At ambient temperature, a coalescence trend was expressed based on (Mori and Wen, 1975) to obtain the height of the transition between the wall and axisymmetric slugs as a function of the

slip velocity (cf. Figure 2) (Gueguen et al., 2022). In the diagrams of Figure 10, this transition appears to follow the same trend. However, not enough results are present in the wall slugging regime in each diagram to fit a coalescence correlation. Nevertheless, there are enough data in each regime to determine the vertical limits between them. Then, the limits between slugging and turbulent fluidization and between turbulent and fast fluidization are represented in the diagrams by vertical black and blue dashed lines, respectively. They have been obtained by maximizing the number of data well identified in their corresponding zones.

Hence, Figure 11 illustrates the influence of temperature on the slugging to turbulent and turbulent to fast fluidization transition limits. Two main trends are clearly identified. First, the transition limits decrease with temperature. The values measured in the range 150-600°C are much lower than the transition limits determined at ambient temperature, of respectively 1.24 and 1.86 for the onset and the termination of the turbulent fluidization regime. Second, the size of the turbulent fluidization domain, i.e., the difference between the two limits, also decreases with temperature.

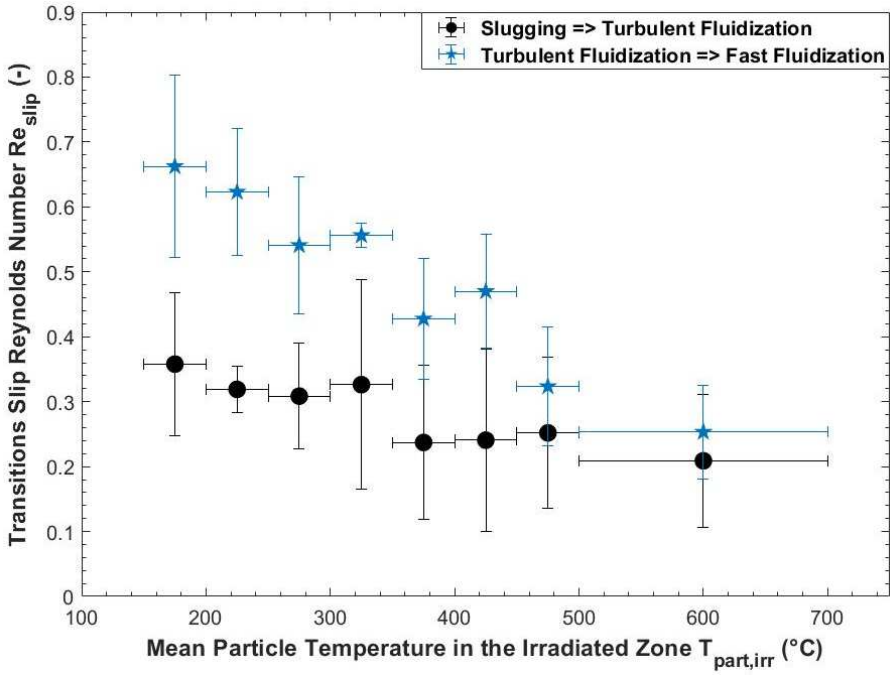

Figure 11: *Evolution of the transition limits between the slugging and turbulent fluidization regimes (black) and between the turbulent and fast fluidization regimes (blue) in terms of the local slip Reynolds number as a function of the mean particle temperature in the irradiated zone.*

4.2. Particle volume fraction

Figure 12 shows the evolution of the local particle volume fraction as a function of the local slip velocity, calculated at the same height. The markers and colors are still representative of the fluidization regimes.

First, the value of α_i is always above 0.2, except for points at very high slip velocities (corresponding to the fast fluidization regime); this result confirms that a dense gas-particle suspension can be maintained regardless of the operation conditions. Second, contrary to the previous section, the slip Reynolds number does not enable the gathering of the points. Hence, this

representation is not detailed here. Although all operation temperatures are represented in the figure, the points are gathered in a decreasing trend using the local slip velocity with a large overlap between the fluidization regimes. Consequently, it appears that the viscous forces do not strongly affect α since the particle volume fraction is a macroscopic parameter that represents the mean particle concentration, averaged in time and space. Conversely, the viscous forces act on the particle mixing at the microscopic level, i.e., on the fluidization regimes.

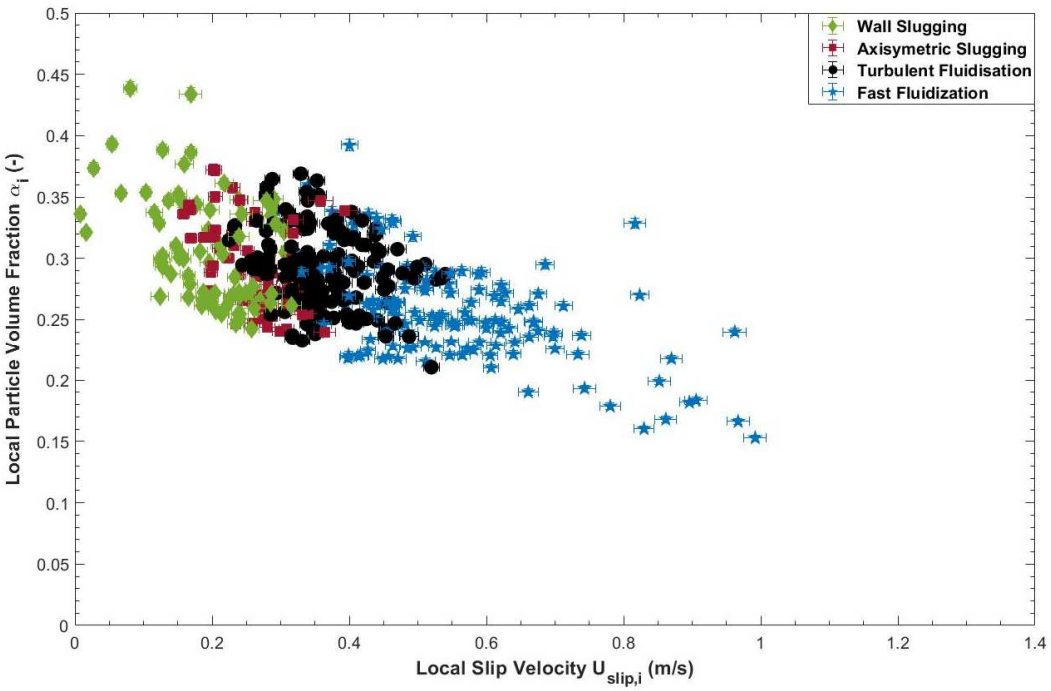

Figure 12: *Evolution of the local particle volume fraction* versus *the local slip velocity, with markers and colors representative of the fluidization regimes, for all tests performed during the experimental campaign.*

Since the air velocity increases with temperature, it is expected that the particle volume fraction also varies with temperature. Figure 13 shows the variation in α_i as a function of the local temperature for the three ranges of the local slip velocity. Decreasing trends are clearly identifiable, which attests that the temperature has a direct and high influence on the particle volume fraction.

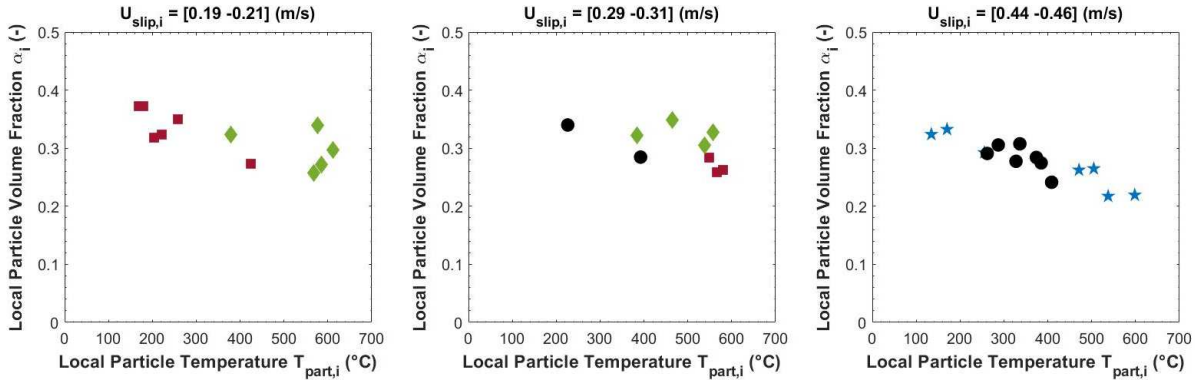

Figure 13: *Evolution of the local particle volume fraction* versus *the local fluidized bed temperature, with markers and colors representative of the fluidization regimes, for three given ranges of the local slip velocity.*

5. Discussion

5.1. Comparison with the literature data

This section aims to compare the results of the fluidization regime transitions with the literature data. This comparison is difficult since most of the studies have been performed only at ambient temperature. However, several transition correlations have been established in terms of the Reynolds number versus the Archimedes number (Equation (12)). They are summarized in Table 3 and are associated with an uncertainty of ± 30%. Since Ar can be calculated as a function of temperature, our data can be compared to the literature. Hence, the transition limits of the onset and termination of the turbulent fluidization regime established in the previous section are plotted in Figure 14 in terms of the slip Reynolds number versus the Archimedes number. In this figure, the points obtained at ambient temperature in the previously cited study (Gueguen et al., 2022) are also identified at high Ar. The slugging to turbulent fluidization transition is in black, and the turbulent to fast fluidization transition is in blue.

$$Ar = \frac{\rho_{air}(\rho_{part} - \rho_{air}) g d_{sv}^3}{\mu_{air}^2} \quad (12)$$

First, (Rabinovich and Kalman, 2011) established correlations for transitions using modified Reynolds numbers that correspond to the product $(1-\alpha)Re_{slip}$. Since the authors provide that values of α of 0.1 and 0.04 in the turbulent and fast fluidization regimes, respectively, corresponding values of the Archimedes number can be calculated. They are presented in Figure 14 with full lines. Then, in the correlations of (Bi and Grace, 1995) and (Deng et al., 2021), the Reynolds number is based on the superficial air velocity. Corresponding slip Reynolds numbers have been calculated according to the data of the experimental parameters provided by the authors, and they are presented in the figure with dashed and dotted lines, respectively. Furthermore, (Zhu and Zhu, 2008) developed the concept of a circulating turbulent fluidized bed as an intermediate between a CFB and a classical fluidized bed working in turbulent fluidization. They did not determine a transition correlation, but they provided enough data to represent their working domain in the figure (black squared). Finally, our results are correlated by the simple Equation (13), where the coefficients are

listed in Table 3. They fit the experimental data at 86% for the slugging to turbulent fluidization transition and 95% for the turbulent to fast fluidization transition. These uncertainties are due to the low quantity of data per temperature range (cf. Figure 10).

$$Re_{slip} = IAr^{J} \tag{13}$$

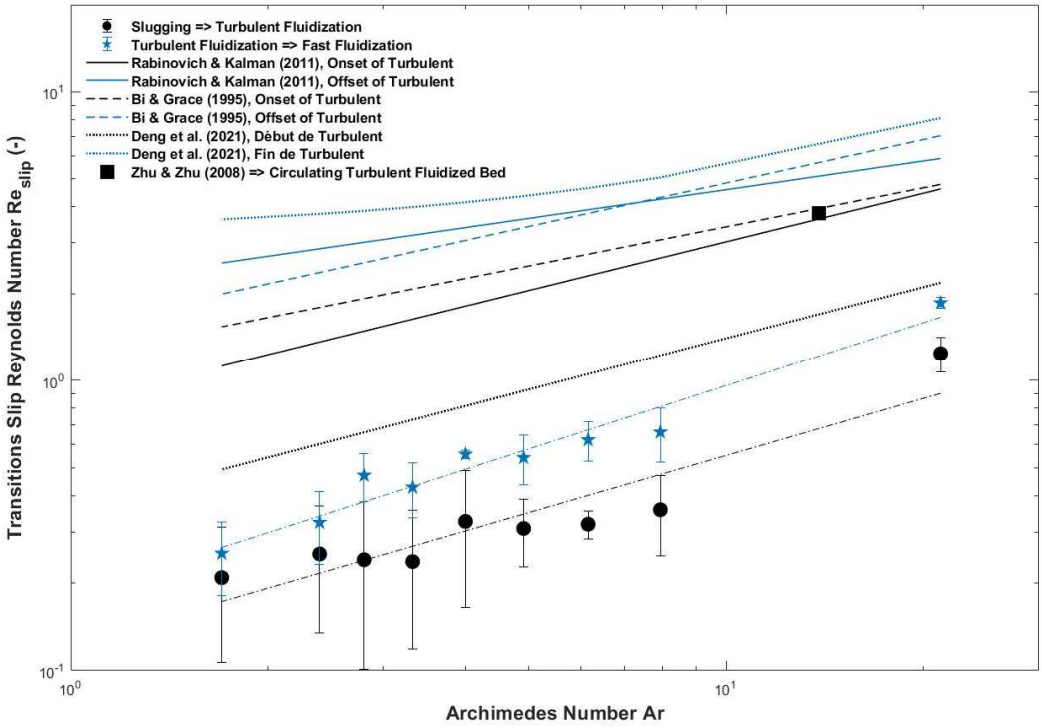

Figure 14: *Comparison of the transition limits from the slugging to the turbulent fluidization regime (black) and from the turbulent to the fast fluidization regime (blue) with the literature data in terms of slip Reynolds number* versus *Archimedes number.*

Table 3: *Correlations established in various studies regarding fluidization regime transitions and in the present paper.*

References	Rabinovich and Kalman, 2011			Bi and Grace, 1995		Deng et al., 2021			This Paper	
Equation of the Transition	$(1-\alpha)Re_{slip} = (A * Ar^{B})$			$Re_{air} = C * Ar^{D}$		$Re_{air} = E * Ar^{F}$		$Re_{air} = G + HAr$		$Re_{slip} = I * Ar^{J}$	
	α	A	B	C	D	E	F	G	H	I	J
Slugging to Turbulent Fluidization	0.1	0.75	0.56	1.21	0.45	0.36	0.59	N.A	N.A	0.12	0.18
Turbulent Fluidization to Fast Fluidization	0.04	2.06	0.33	1.53	0.50	N.A	N.A	3.23.	0.23	0.65	0.73

Our results are significantly lower than the literature data. This is mostly due to the operation mode of the system. Moreover, in the particle-in-tube solar receiver concept, the particle circulation

669 is controlled by both the overpressure in the dispenser and the aeration flow rate. Consequently,
670 part of the energy needed to create the particle circulation in a given flow regime is provided by the
671 overpressure, as demonstrated in (Zhang et al., 2017b). In contrast, the circulation in CFBs is only due
672 to a high air velocity (one order of magnitude larger than our). Then, in CFBs, the particle volume
673 fractions in the turbulent and fast fluidization regimes are very low, while they remain relatively
674 dense in our experiments with values above 0.15 even in the fast fluidization regime (cf. Figure 12).
675 In addition, Figure 14 indicates that the turbulent fluidization domain decreases with decreasing Ar,
676 i.e., with increasing temperature, in agreement with the data from (Bi and Grace, 1995). Conversely,
677 the correlations of (Rabinovich and Kalman, 2011) and (Deng et al., 2021) predict an opposite trend.

678 Despite the differences with the literature data, the transition trends are similar. The trends
679 are relatively linear using logarithmic scales, and the slopes are positive. Therefore, the Archimedes
680 number appears to be the pertinent number that accounts for the temperature effect on the
681 fluidization regimes and their transitions.

682

683 ## 5.2. Wall-to-fluidized bed heat transfer

684 A relevant quantity for designing a solar receiver and characterizing its thermal performance,
685 accounting for the wall material specifications and the solar concentrating system, is the wall-to-
686 particle heat transfer coefficient, noted $h_{wall,part}$ and calculated by Equation (14) (Benoit et al.,
687 2015; Le Gal et al., 2019). In this equation, the heat capacity $C_{p,part}$ is calculated as a function of the
688 particle temperature according to (Kang et al., 2019; Le Gal et al., 2019) and varies between 1 and
689 1.22 kJ/(kgK) in our experimental temperature range. The particle temperature increase, ΔT_{part}, is
690 selected as the difference between the particle temperatures at the outlet of the receiver and in the
691 dispenser to describe the real increase due to solar irradiation. The surface exchange area S_{exch} is
692 half of the internal cylinder surface since it accounts for the heat transfer from the irradiated part of
693 the tube only. Finally, $\Delta T_{wall,part}$ represents the temperature difference between the internal walls
694 and the particles. This difference is expressed as a logarithmic mean between the inlet and the outlet
695 of the irradiated height (Equation (15)), similar to the power balance in heat exchangers. The particle
696 inlet temperature is calculated as the average of the temperatures measured within the tube at the
697 inlet of the irradiated zone, in the same way as T_{part}^{out} is measured (cf. Section 3): $T_{part}^{in} =$
698 $\left(T_{int,4} + T_{int,5} + T_{int,9}\right)/3$, where the thermocouples are at radial positions of $D_t/3$, $D_t/2$ and
699 $2D_t/3$. The calculation requires the determination of the internal wall temperatures at the inlet and
700 outlet of the irradiated zone, respectively $T_{wall,int}^{in}$ and $T_{wall,int}^{out}$. These are not directly measured but
701 can be estimated based on the external wall temperature measurements, $T_{wall,ext}^{in}$ and $T_{wall,ext}^{out}$,
702 considering the heat conduction through the tube (Equation (16)). The thermal conductivity of the
703 Inconel $\lambda_{inconel}$ is a function of the temperature according to ("Alloy Wire International, Inconel
704 601," 2020) and varies between 14.6 and 25.6 W/(mK). In addition, the absorptivity of the Pyromark®
705 paint $\alpha_{pyromark}$ is 0.85 in the solar wavelengths according to (C. K. Ho et al., 2014), and e_t is the
706 tube thickness of 3 mm.

707

$$h_{wall,part} = \frac{G_p S_t C_{p,part} \Delta T_{part}}{S_{exch} \Delta T_{wall,part}} \tag{14}$$

$$\Delta T_{wall,part} = \frac{\left(T_{wall,int}^{in} - T_{part}^{in}\right) - \left(T_{wall,int}^{out} - T_{part}^{out}\right)}{\ln\left(\frac{T_{wall,int}^{in} - T_{part}^{in}}{T_{wall,int}^{out} - T_{part}^{out}}\right)} \quad (15)$$

$$T_{wall,int}^{in,out} = T_{wall,ext}^{in,out} - \frac{e_t}{\lambda_{inconel}} \alpha_{pyromark} \varphi_{sol} \quad (16)$$

708

709 The wall-to-particle heat transfer coefficient, $h_{wall,part}$, is presented in Figure 15a for several
710 fluidization regimes and three particle temperature ranges. Values up to 1600 ± 200 W/(m².K) were
711 measured during the experimental campaign. Due to the definition of $h_{wall,part}$ (in Equation (14)), it
712 is strongly dependent on the particle mass flux, as previously shown by (Benoit et al., 2015; Le Gal et
713 al., 2019). Since high particle temperatures have been obtained for low particle mass fluxes because
714 of constraints related to the experimental setup limitations at the laboratory scale, they are
715 associated with low values of $h_{wall,part}$, and there is no identifiable dependence on the fluidization
716 regime. Consequently, it does not qualitatively show the quality of the heat transfer between the
717 wall and the particles, which strongly depends on the particle mixing, i.e., on the fluidization regime.

718 In an ideal solar receiver, the temperature of the particles would be equal to the tube wall;
719 hence, $\Delta T_{wall,part}$ would be null, and the particle temperature increase ΔT_{part} would be maximum,
720 causing the wall-to-particle heat transfer coefficient to be infinite. Then, a dimensionless heat
721 transfer coefficient, $H_{wall,part}$, is derived. It is calculated by Equation (17) as a ratio of the particle
722 temperature increase over the mean temperature difference between the internal wall and the
723 particles. Hence, it is infinite in the case of an ideal receiver and is an indicator of the heat transfer
724 quality, or its intensity.

725

$$H_{wall,part} = \frac{\Delta T_{part}}{\Delta T_{wall,part}} = \frac{h_{wall,part} S_{exch}}{G_p S_t C_{p,part}} \quad (17)$$

726

727 According to (Grace et al., 2020c), the heat transfer in a fluidized bed is composed of
728 convective, conductive and radiative components that increase with the bed temperature. The same
729 trend is illustrated in Figure 15b, which represents the mean values of the dimensionless wall-to-
730 particle heat transfer coefficient for the same conditions as previously described.

731 First, it is clearly observed that the quality of the heat transfer increases with the particle
732 temperature, as expected. Furthermore, at low temperature, the values of dimensionless $H_{wall,part}$
733 are similar for the slugging, turbulent and fast fluidization regimes. When the temperature increases,
734 the turbulent fluidization regime is associated with the highest dimensionless heat transfer
735 coefficients, while the slugging regime exhibits lowest $H_{wall,part}$ values. Moreover, the very high
736 particle mixing and the medium particle volume fraction associated with the turbulent fluidization
737 regime results in highly efficient heat transfer.

738

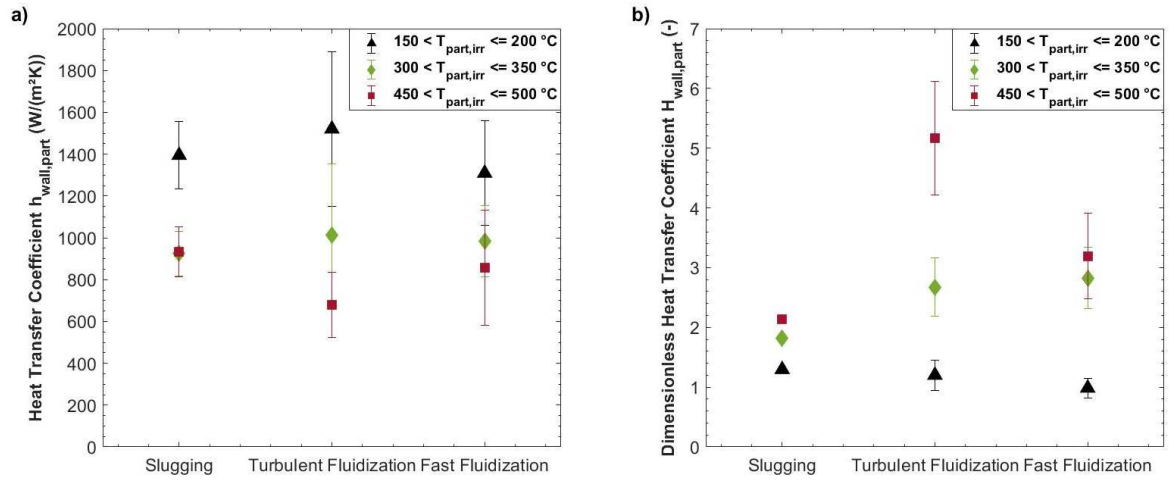

Figure 15: *Evolution of the wall-to-particle heat transfer coefficient, a) in a common representation (in W/(m².K)) and b) as a dimensionless coefficient, for the slugging, turbulent and fast fluidization regimes at a given particle temperature.*

5.3. The role of temperature in the regime transition and the associated heat transfer

As pointed in (Cui et al., 2003), the effect of temperature on fluidized Group A particles flow cannot be fully explained by the macro-scale change of gas properties (density and viscosity), micro-scale changes are also important. Geldart's Group A particles are subjected to clustering contrarily to Group B as shown in (Leckner, 2017) who compared the behavior of Geldart's Group A and B. Clustering is due to inter-particle forces that gain importance for small particles (Group A). Since the temperature increase results in weaker attraction forces, the particle volume fraction decreases (the bed porosity increases) with temperature as shown in (Formisani et al., 1998). On this basis, the following explanation of the decrease with temperature of the transition velocity between slugging to turbulent regime and between turbulent to fast fluidization regimes is proposed (Figure 11). The increase in temperature results in particles that are more distant in the dense phase, consequently, emulsion phase and clusters break more easily with a rise in gas velocity. This effect becomes more important at high gas velocity since inertia forces increases with respect to viscous forces that dominate at low velocity. This trend explains the narrowing of the turbulent regime domain. This interpretation is supported by the work of (Choi et al., 2011).

Concerning the effect of the temperature and the fluidization regime on the heat transfer coefficient, $H_{wall,part}$ (Figure 15) the following interpretation is proposed. First, the increase of $H_{wall,part}$ with the temperature is well established since both the air thermal conductivity and the radiation contribution increase with the temperature (Flamant et al., 1993). Second, the surface-particle-emulsion model is a coherent basis to explain the influence of fluidization regime (Wang et al., 2007). Assuming that the heat transfer between a fluidized bed and an immersed surface is governed by the dynamic process of heat exchange between emulsion packets or particle clusters (particle phase) that are continuously renewed at the surface; one can easily deduce that the exchange efficiency depends on the particle phase properties and its residence time. The heat exchange intensity is high for low residence time (fast renewal) and high particle phase density (high equivalent thermal diffusivity). The turbulent regime is a tradeoff between long residence time in the slugging regime and lean cluster phase in the fast fluidization regime. It corresponds to an intense renewal of dense particle clusters at the heat exchange surface.

6. Conclusion

The evolution of the hydrodynamics of an upward-flowing fluidized bed in a tubular solar receiver with a high aspect ratio is assessed as a function of temperature. Olivine particles belonging to Group A of the Geldart classification are used. The superficial air velocity in the tube varies between 0.025 and 0.469 m/s, and the particle mass flux ranges between 0 and 93 kg/(m².s). The tube is heated due to concentrated solar energy, causing the particle temperature at the outlet of the receiver to reach 680 °C.

Temporal pressure signal analyses are used to identify the fluidization regimes in the tube. Bubbling, wall and axisymmetric slugging, turbulent fluidization and fast fluidization are identified. Their transitions are governed by both the local slip velocity, expressed as a particle Reynolds number to account for the viscous effects, and the particle temperature. The onset and offset limits of the turbulent fluidization regime both decrease with temperature. The transition velocities are significantly lower than those for the standard CFB and C-TFB, probably due to the two forces (pressure and drag components) governing the flow structure.

The local particle volume fraction decreases with both the slip velocity and the particle temperature and remains above 15–20%. Consequently, the fluidized bed can be considered dense regardless of the fluidization regime.

A dimensionless wall-to-particle heat transfer coefficient is derived to determine the intensity of the heat transfer. The heat transfer coefficient increases with the temperature. Furthermore, the turbulent fluidization regime is associated with the highest heat transfer intensity. Thus, this regime should be preferred for the operation of a solar power plant.

Acknowledgements

The characterization of the olivine sample was conducted with the help of the Material Characterization Platform – Surfaces and Interfaces Analyses of the PROMES (CNRS) laboratory. Regis Rodriguez and Alex Le Gal are thanked for their help with the LabVIEW acquisition software. Finally, the authors would like to thank Michael Tessoneaud and Guillaume Sahuquet for their help carrying out the experiments.

Funding

This work was funded by the French “Investments for the future” (“*Investissements d’Avenir*”) program managed by the National Agency for Research (ANR) under contract ANR-10-LABX-22-01 (labex SOLSTICE).

Nomenclature

Abbreviations

CFB	Circulating Fluidized Bed
C-TFB	Circulating-turbulent fluidized bed
CSP	Concentrated Solar Power
HTF	Heat Transfer Fluid
I.D.	Internal diameter

Arabic letters

Ar	Archimedes number (Ø)
$C_{p,part}$	Particle heat capacity (kJ/(kgK))
d_{sv}	Powder Sauter diameter (µm)
D_t	Tube internal diameter (m)
e_t	Tube thickness (mm)
g	Standard gravity (m/s²)
G_p	Particle mass flux (kg/(m².s))
H_t	Tube height (m)
$h_{wall,part}$	Wall-to-particle heat transfer coefficient (W/(m².K))
$H_{wall,part}$	Dimensionless wall-to-particle heat transfer coefficient (Ø)
P_{tot}	Relative pressure in the dispenser (mbar)
$\dot{q_{ae}}$	Aeration flow rate (sm^3/h)
Re_{slip}	Reynolds slip number (Ø)
S_t	Internal tube section (m²)
T_{disp}	Temperature in the dispenser (°C)
T_{part}^{in}	Particle temperature at the inlet of the irradiated zone of the tube (°C)
T_{part}^{out}	Particle temperature at the outlet of the irradiated zone of the tube (°C)
$T_{part,irr}$	Mean particle temperature over the irradiated zone of the tube (°C)
$T_{wall,int}$	Internal tube temperature (°C)
$T_{wall,ext}$	External tube temperature (°C)
U_{air}	Superficial air velocity (m/s)
U_k	Fast fluidization velocity (m/s)
U_{mb}	Minimum bubbling velocity (m/s)
U_{mf}	Minimum fluidization velocity (m/s)

839	U_{ms}	Minimum slugging velocity (m/s)
840	U_{slip}	Slip velocity (m/s)
841	U_t	Turbulent fluidization velocity (m/s)
842		
843	*Greek letters*	
844	α	Particle volume fraction (Ø)
845	φ_{sol}	Incident concentrated solar flux density (kW/m²)
846	μ_{air}	Air viscosity (kg/m/s)
847	ρ_{air}	Air density (kg/m^3)
848	ρ_{part}	Particle density (kg/m^3)

849

850 References

851 Abrahamsen, A.R., Geldart, D., 1980. Behaviour of gas-fluidized beds of fine powders part I.
852 Homogeneous expansion. Powder Technology 26, 35–46. https://doi.org/10.1016/0032-
853 5910(80)85005-4

854 Alloy Wire International, Inconel 601 [WWW Document], 2020. URL
855 www.alloywire.fr/products/inconel-601 (accessed 9.11.20).

856 Baeyens, J., Geldart, D., 1974. An investigation into slugging fluidized beds. Chemical Engineering
857 Science 29, 255–265. https://doi.org/10.1016/0009-2509(74)85051-7

858 Behar, O., Grange, B., Flamant, G., 2020. Design and performance of a modular combined cycle solar
859 power plant using the fluidized particle solar receiver technology. Energy Conversion and
860 Management 220, 113108. https://doi.org/10.1016/j.enconman.2020.113108

861 Benoit, H., Ansart, R., Neau, H., Garcia Triñanes, P., Flamant, G., Simonin, O., 2018. Three-
862 dimensional numerical simulation of upflow bubbling fluidized bed in opaque tube under
863 high flux solar heating. AIChE J 64, 3857–3867. https://doi.org/10.1002/aic.16218

864 Benoit, H., Pérez López, I., Gauthier, D., Sans, J.-L., Flamant, G., 2015. On-sun demonstration of a 750
865 °C heat transfer fluid for concentrating solar systems: Dense particle suspension in tube.
866 Solar Energy 118, 622–633. https://doi.org/10.1016/j.solener.2015.06.007

867 Bi, H.T., 2007. A critical review of the complex pressure fluctuation phenomenon in gas–solids
868 fluidized beds. Chemical Engineering Science 62, 3473–3493.
869 https://doi.org/10.1016/j.ces.2006.12.092

870 Bi, H.T., Ellis, N., Abba, I.A., Grace, J.R., 2000. A state-of-the-art review of gas–solid turbulent
871 fluidization. Chemical Engineering Science 55, 4789–4825. https://doi.org/10.1016/S0009-
872 2509(00)00107-X

873 Bi, H.T., Grace, J.R., 1995. Flow regime diagrams for gas-solid fluidization and upward transport.
874 International Journal of Multiphase Flow 21, 1229–1236. https://doi.org/10.1016/0301-
875 9322(95)00037-X

Bi, H.T., Grace, J.R., Zhu, J.-X., 1993. Types of choking in vertical pneumatic systems. International Journal of Multiphase Flow 19, 1077–1092. https://doi.org/10.1016/0301-9322(93)90079-A

Boissiere, B., Ansart, R., Gauthier, D., Flamant, G., Hemati, M., 2015. Experimental hydrodynamic study of gas-particle dense suspension upward flow for application as new heat transfer and storage fluid. Can. J. Chem. Eng. 93, 317–330. https://doi.org/10.1002/cjce.22087

Boonprasop, S., Chalermsinsuwan, B., Piumsomboon, P., 2019. Circulating turbulent fluidized bed regime on flow regime diagram. Powder Technology 350, 146–153. https://doi.org/10.1016/j.powtec.2019.03.047

Breault, R.W., Weber, J., Shadle, L.J., 2020. The development of a generalized riser flow regime map based upon higher moment and chaotic statistics using electrical capacitance volume tomography (ECVT). Powder Technology 365, 12–27. https://doi.org/10.1016/j.powtec.2019.03.036

Castro-Quijada, M., Faundez, D., Rojas, R., Videla, A., 2022. Improving the working fluid based on a NaNO3-KNO3-NaCl-KCl molten salt mixture for concentrating solar power energy storage. Solar Energy 231, 464–472. https://doi.org/10.1016/j.solener.2021.11.058

Choi, J.-H., Ryu, H.-J., Yi, C.-K., 2011. A model for the temperature effect on onset velocity of turbulent fluidization of Geldart type A particles. Korean J. Chem. Eng. 28, 304–307. https://doi.org/10.1007/s11814-010-0337-x

Cui, H., Sauriol, P., Chaouki, J., 2003. High temperature fluidized bed reactor: measurements, hydrodynamics and simulation. Chemical Engineering Science 58, 1071–1077. https://doi.org/10.1016/S0009-2509(02)00649-8

Deng, Y., Sabatier, F., Dewil, R., Flamant, G., Le Gal, A., Gueguen, R., Baeyens, J., Li, S., Ansart, R., 2021. Dense upflow fluidized bed (DUFB) solar receivers of high aspect ratio: Different fluidization modes through inserting bubble rupture promoters. Chemical Engineering Journal 418, 129376. https://doi.org/10.1016/j.cej.2021.129376

Dodds, J., Baluais, G., 1993. Caractérisation de la taille des particules. Particle size characterization. sgeol 46, 79–104. https://doi.org/10.3406/sgeol.1993.1898

Dunham, M.T., Iverson, B.D., 2014. High-efficiency thermodynamic power cycles for concentrated solar power systems. Renewable and Sustainable Energy Reviews 30, 758–770. https://doi.org/10.1016/j.rser.2013.11.010

Ebert, M., Amsbeck, L., Rheinländer, J., Schlögl-Knothe, B., Schmitz, S., Sibum, M., Uhlig, R., Buck, R., 2019. Operational experience of a centrifugal particle receiver prototype. Presented at the SOLARPACES 2018: International Conference on Concentrating Solar Power and Chemical Energy Systems, Casablanca, Morocco, p. 030018. https://doi.org/10.1063/1.5117530

Fan, L.T., Ho, T.-C., Walawender, W.P., 1983. Measurements of the rise velocities of bubbles, slugs and pressure waves in a gas-solid fluidized bed using pressure fluctuation signals. AIChE J. 29, 33–39. https://doi.org/10.1002/aic.690290105

Flamant, G., Gauthier, D., Benoit, H., Sans, J.-L., Garcia, R., Boissière, B., Ansart, R., Hemati, M., 2013. Dense suspension of solid particles as a new heat transfer fluid for concentrated solar thermal plants: On-sun proof of concept. Chemical Engineering Science 102, 567–576. https://doi.org/10.1016/j.ces.2013.08.051

Flamant, G., Lu, J.D., Variot, B., 1993. Towards a generalized model for vertical walls to gas—solid fluidized beds heat transfer—II. Radiative transfer and temperature effects. Chemical Engineering Science 48, 2493–2503. https://doi.org/10.1016/0009-2509(93)81070-C

Formisani, B., Girimonte, R., Mancuso, L., 1998. Analysis of the fluidization process of particle beds at high temperature. Chemical Engineering Science 53, 951–961. https://doi.org/10.1016/S0009-2509(97)00370-9

Fuchs, J., Schmid, J.C., Müller, S., Hofbauer, H., 2019. Dual fluidized bed gasification of biomass with selective carbon dioxide removal and limestone as bed material: A review. Renewable and Sustainable Energy Reviews 107, 212–231. https://doi.org/10.1016/j.rser.2019.03.013

Geldart, D., 1986. Chap. 4: Hydrodynamics of Bubbling Fluidized Beds, in: Gas Fluidization Technology. John Wiley & Sons Ltd.: Chichester, U.K., pp. 53–96.

Geldart, D., 1973. Types of gas fluidization. Powder Technology 7, 285–292. https://doi.org/10.1016/0032-5910(73)80037-3

Grace, J.R., Bi, X., Ellis, N., 2020a. Chap. 9: Turbulent Fluidization, in: Essential of Fluidization Technology. John Wiley & Sons Ltd.: Chichester, U.K., pp. 163–180.

Grace, J.R., Bi, X., Ellis, N., 2020b. Chap. 4: Gas Fluidization Flow Regimes, in: Essential of Fluidization Technology. John Wiley & Sons Ltd.: Chichester, U.K., pp. 55–74.

Grace, J.R., Bi, X., Ellis, N., 2020c. Chap. 14: Heat and Mass Transfer, in: Essential of Fluidization Technology. John Wiley & Sons Ltd.: Chichester, U.K., pp. 291–332.

Gueguen, R., Grange, B., Bataille, F., Mer, S., Flamant, G., 2020. Shaping High Efficiency, High Temperature Cavity Tubular Solar Central Receivers. Energies 13, 4803. https://doi.org/10.3390/en13184803

Gueguen, R., Sahuquet, G., Mer, S., Toutant, A., Bataille, F., Flamant, G., 2022. Fluidization Regimes of Dense Suspensions of Geldart Group A Fluidized Particles in a High Aspect Ratio Column. Chemical Engineering Science 118360. https://doi.org/10.1016/j.ces.2022.118360

Gueguen, R., Sahuquet, G., Mer, S., Toutant, A., Bataille, F., Flamant, G., 2021. Gas-Solid Flow in a Fluidized-Particle Tubular Solar Receiver: Off-Sun Experimental Flow Regimes Characterization. Energies 14, 7392. https://doi.org/10.3390/en14217392

Guillot, E., Rodriguez, R., Boullet, N., Sans, J.-L., 2018. ARGOS: Solar furnaces flat heliostats tracking error estimation with a direct camera-based vision system. Presented at the SolarPACES 2017: International Conference on Concentrating Solar Power and Chemical Energy Systems, Santiago, Chile, p. 200001. https://doi.org/10.1063/1.5067202

Ho, C., Christian, J., Gill, D., Moya, A., Jeter, S., Abdel-Khalik, S., Sadowski, D., Siegel, N., Al-Ansary, H., Amsbeck, L., Gobereit, B., Buck, R., 2014. Technology Advancements for Next Generation Falling Particle Receivers. Energy Procedia 49, 398–407. https://doi.org/10.1016/j.egypro.2014.03.043

Ho, C.K., 2016. A review of high-temperature particle receivers for concentrating solar power. Applied Thermal Engineering 109, 958–969. https://doi.org/10.1016/j.applthermaleng.2016.04.103

Ho, C.K., Christian, J., Yellowhair, J., Jeter, S., Golob, M., Nguyen, C., Repole, K., Abdel-Khalik, S., Siegel, N., Al-Ansary, H., El-Leathy, A., Gobereit, B., 2017. Highlights of the high-temperature falling particle receiver project: 2012 - 2016. Presented at the SOLARPACES 2016: International Conference on Concentrating Solar Power and Chemical Energy Systems, Abu Dhabi, United Arab Emirates, p. 030027. https://doi.org/10.1063/1.4984370

Ho, C.K., Mahoney, A.R., Ambrosini, A., Bencomo, M., Hall, A., Lambert, T.N., 2014. Characterization of Pyromark 2500 Paint for High-Temperature Solar Receivers. Journal of Solar Energy Engineering 136, 014502. https://doi.org/10.1115/1.4024031

964 Holman, J.P., 2002. Heat transfer, International ed., 9. ed. ed, McGraw-Hill series in mechanical
965 engineering. McGraw-Hill, Boston London.

966 Incropera, F.P., DeWitt, D.P., Bergman, T.L., Lavine, A.S. (Eds.), 2007. Fundamentals of heat and mass
967 transfer, 6. ed. ed. Wiley, Hoboken, NJ.

968 Johnsson, F., Zijerveld, R.C., Schouten, J.C., van den Bleek, C.M., Leckner, B., 2000. Characterization of
969 fluidization regimes by time-series analysis of pressure fluctuations. International Journal of
970 Multiphase Flow 26, 663–715. https://doi.org/10.1016/S0301-9322(99)00028-2

971 Kang, Q., Flamant, G., Dewil, R., Baeyens, J., Zhang, H.L., Deng, Y.M., 2019. Particles in a circulation
972 loop for solar energy capture and storage. Particuology 43, 149–156.
973 https://doi.org/10.1016/j.partic.2018.01.009

974 Kong, W., Tan, T., Baeyens, J., Flamant, G., Zhang, H., 2017. Bubbling and Slugging of Geldart Group A
975 Powders in Small Diameter Columns. Ind. Eng. Chem. Res. 56, 4136–4144.
976 https://doi.org/10.1021/acs.iecr.6b04798

977 Kunii, D., Levenspiel, O., 1991. Chap. 3: Fluidization and Mapping of Regimes, in: Fluidization
978 Engineering. Elsevier, pp. 61–94. https://doi.org/10.1016/B978-0-08-050664-7.50009-3

979 Le Gal, A., Grange, B., Casanova, M., Perez, A., Baltus, W., Tessonneaud, M., Flamant, G., 2023.
980 Experimental results for a MW-scale fluidized particle-in-tube solar receiver in its first test
981 campaign. Solar Energy 262, 111907. https://doi.org/10.1016/j.solener.2023.111907

982 Le Gal, A., Grange, B., Tessonneaud, M., Perez, A., Escape, C., Sans, J.-L., Flamant, G., 2019. Thermal
983 analysis of fluidized particle flows in a finned tube solar receiver. Solar Energy 191, 19–33.
984 https://doi.org/10.1016/j.solener.2019.08.062

985 Leckner, B., 2017. Regimes of large-scale fluidized beds for solid fuel conversion. Powder Technology
986 308, 362–367. https://doi.org/10.1016/j.powtec.2016.11.070

987 Li, Y., Grace, J.R., Gopaluni, R.B., Bi, H., Lim, C.J., Ellis, N., 2011. Characterization of gas–solid
988 fluidization: A comparative study of acoustic and pressure signals. Powder Technology 214,
989 200–210. https://doi.org/10.1016/j.powtec.2011.08.009

990 Mokhtari, M., Chaouki, J., 2019. New technique for simultaneous measurement of the local solid and
991 gas holdup by using optical fiber probes in the slurry bubble column. Chemical Engineering
992 Journal 358, 831–841. https://doi.org/10.1016/j.cej.2018.10.067

993 Mori, S., Wen, C.Y., 1975. Estimation of bubble diameter in gaseous fluidized beds. AIChE J. 21, 109–
994 115. https://doi.org/10.1002/aic.690210114

995 Next-CSP Project: High Temperature Concentrated Solar Thermal Plant with Particle Receiver and
996 Direct Thermal Storage [WWW Document], 2020. URL
997 https://cordis.europa.eu/project/id/727762 (accessed 12.12.22).

998 Nigmetova, A., Masi, E., Simonin, O., Dufresne, Y., Moureau, V., 2022. Three-dimensional DEM-CFD
999 simulation of a lab-scale fluidized bed to support the development of two-fluid model
1000 approach. International Journal of Multiphase Flow 156, 104189.
1001 https://doi.org/10.1016/j.ijmultiphaseflow.2022.104189

1002 Perez Lopez, I., Benoit, H., Gauthier, D., Sans, J.L., Guillot, E., Mazza, G., Flamant, G., 2016. On-sun
1003 operation of a 150 kWth pilot solar receiver using dense particle suspension as heat transfer
1004 fluid. Solar Energy 137, 463–476. https://doi.org/10.1016/j.solener.2016.08.034

1005 Plancherel, M., Leffler, M., 1910. Contribution à l'étude de la représentation d'une fonction arbitraire
1006 par des intégrales définies. Rend. Circ. Matem. Palermo 30, 289–335.
1007 https://doi.org/10.1007/BF03014877

1008 Price, J., Goble, T., 1993. Signals and noise, in: Telecommunications Engineer's Reference Book.
1009 Elsevier, pp. 10-1-10–15. https://doi.org/10.1016/B978-0-7506-1162-6.50016-2

1010 Punčochář, M., Drahoš, J., 2005. Origin of pressure fluctuations in fluidized beds. Chemical
1011 Engineering Science 60, 1193–1197. https://doi.org/10.1016/j.ces.2004.09.054

1012 Rabinovich, E., Kalman, H., 2011. Flow regime diagram for vertical pneumatic conveying and fluidized
1013 bed systems. Powder Technology 207, 119–133.
1014 https://doi.org/10.1016/j.powtec.2010.10.017

1015 Rahman, M.H., Bi, X.T., Grace, J.R., Lim, C.J., 2020. Comparison of techniques for measuring CFB
1016 solids circulation rates at low and high temperatures. Powder Technology 360, 43–54.
1017 https://doi.org/10.1016/j.powtec.2019.10.033

1018 Sabatier, F., Ansart, R., Zhang, H., Baeyens, J., Simonin, O., 2020. Experiments support simulations by
1019 the NEPTUNE_CFD code in an Upflow Bubbling Fluidized Bed reactor. Chemical Engineering
1020 Journal 385, 123568. https://doi.org/10.1016/j.cej.2019.123568

1021 Shaffer, F., Gopalan, B., Breault, R.W., Cocco, R., Karri, S.B.R., Hays, R., Knowlton, T., 2013. High
1022 speed imaging of particle flow fields in CFB risers. Powder Technology 242, 86–99.
1023 https://doi.org/10.1016/j.powtec.2013.01.012

1024 Shannon, C.E., 1949. Communication in the Presence of Noise. Proc. IRE 37, 10–21.
1025 https://doi.org/10.1109/JRPROC.1949.232969

1026 Stefanova, A., Bi, H.T., Lim, J.C., Grace, J.R., 2011. Local hydrodynamics and heat transfer in fluidized
1027 beds of different diameter. Powder Technology 212, 57–63.
1028 https://doi.org/10.1016/j.powtec.2011.04.026

1029 Sun, Z., Zhu, J., 2021. A four-quadrant flow regime map for two-phase liquid-solids and gas-solids
1030 fluidization systems. Powder Technology 394, 424–438.
1031 https://doi.org/10.1016/j.powtec.2021.08.050

1032 Sun, Z., Zhu, J., 2019. A consolidated flow regime map of upward gas fluidization. AIChE J 65.
1033 https://doi.org/10.1002/aic.16672

1034 Tebianian, S., Dubrawski, K., Ellis, N., Cocco, R.A., Hays, R., Karri, S.B.R., Leadbeater, T.W., Parker, D.J.,
1035 Chaouki, J., Jafari, R., Garcia-Trinanes, P., Seville, J.P.K., Grace, J.R., 2016. Solids flux
1036 measurements via alternate techniques in a gas-fluidized bed. Chemical Engineering Journal
1037 306, 306–321. https://doi.org/10.1016/j.cej.2016.07.058

1038 Trombe, F., Albert Le Phat Vinh, 1973. Thousand kW solar furnace, built by the National Center of
1039 Scientific Research, in Odeillo (France). Solar Energy 15, 57–61.
1040 https://doi.org/10.1016/0038-092X(73)90006-6

1041 Van de Velden, M., Baeyens, J., Seville, J.P.K., Fan, X., 2008. The solids flow in the riser of a Circulating
1042 Fluidised Bed (CFB) viewed by Positron Emission Particle Tracking (PEPT). Powder Technology
1043 183, 290–296. https://doi.org/10.1016/j.powtec.2007.07.027

1044 van der Schaaf, J., Schouten, J.C., Johnsson, F., van den Bleek, C.M., 2002. Non-intrusive
1045 determination of bubble and slug length scales in fluidized beds by decomposition of the
1046 power spectral density of pressure time series. International Journal of Multiphase Flow 28,
1047 865–880. https://doi.org/10.1016/S0301-9322(01)00090-8

1048 Villa Briongos, J., Aragón, J.M., Palancar, M.C., 2006. Fluidised bed dynamics diagnosis from
1049 measurements of low-frequency out-bed passive acoustic emissions. Powder Technology
1050 162, 145–156. https://doi.org/10.1016/j.powtec.2005.12.009

Wang, L., Wu, P., Yang, J., Ni, X., 2007. Modeling of heat transfer between a high-temperature fluidized bed and an immersed surface by a surface-particle-emulsion model. Chemical Engineering Science 62, 503–512. https://doi.org/10.1016/j.ces.2006.09.018

Wu, S.Y., Baeyens, J., 1991. Effect of operating temperature on minimum fluidization velocity. Powder Technology 67, 217–220. https://doi.org/10.1016/0032-5910(91)80158-F

Wu, W., Amsbeck, L., Buck, R., Uhlig, R., Ritz-Paal, R., 2014. Proof of Concept Test of a Centrifugal Particle Receiver. Energy Procedia 49, 560–568. https://doi.org/10.1016/j.egypro.2014.03.060

Xie, H.-Y., 1997. Pressure probes in the measurement of bubble properties in the fluidization of fine particles. Advanced Powder Technology 8, 217–235. https://doi.org/10.1016/S0921-8831(08)60464-1

Yerushalmi, J., Cankurt, N.T., 1979. Further studies of the regimes of fluidization. Powder Technology 24, 187–205. https://doi.org/10.1016/0032-5910(79)87036-9

Zhang, H., Benoit, H., Perez-Lopèz, I., Flamant, G., Tan, T., Baeyens, J., 2017a. High-efficiency solar power towers using particle suspensions as heat carrier in the receiver and in the thermal energy storage. Renewable Energy 111, 438–446. https://doi.org/10.1016/j.renene.2017.03.101

Zhang, H., Kong, W., Tan, T., Gilles, F., Baeyens, J., 2017b. Experiments support an improved model for particle transport in fluidized beds. Sci Rep 7, 10178. https://doi.org/10.1038/s41598-017-10597-3

Zhang, H.L., Degrève, J., Dewil, R., Baeyens, J., 2015. Operation Diagram of Circulating Fluidized Beds (CFBs). Procedia Engineering 102, 1092–1103. https://doi.org/10.1016/j.proeng.2015.01.232

Zhou, L., 2023. A review for measurements and simulations of swirling gas-particle flows. Exp. Comput. Multiph. Flow 5, 133–141. https://doi.org/10.1007/s42757-021-0109-3

Zhu, H., Zhu, J., 2008. Comparative study of flow structures in a circulating-turbulent fluidized bed. Chemical Engineering Science 63, 2920–2927. https://doi.org/10.1016/j.ces.2008.03.022